3-8

(NASA-CR-112057) HYPERSONIC RESEARCH ENGINE PROJECT. PHASE 2: STRUCTURES AND COOLING DEVELOPMENT Interim L.F. Jilly (AiResearch Mfg. Co., Los Angeles, Calif.) 18 Mar. 1971 85 p

N72-24819

CSCL 21H G3/28

Unclas 28793

GARRETT

AIRESEARCH MANUFACTURING COMPANY

A DIVISION OF THE GARRETT CORPORATION

9851-9951 SEPULVEDA BLVD. • LOS ANGELES, CALIFORNIA 90009

TELEPHONE: SPRING 6-1010, ORCHARD 0-0131 • CABLE: GARRETTAIR LOS ANGELES

AIRESEARCH MANUFACTURING COMPANY

Los Angeles, California

HYPERSONIC RESEARCH ENGINE PROJECT - PHASE II
STRUCTURES AND COOLING DEVELOPMENT
SIXTEENTH INTERIM TECHNICAL DATA REPORT
DATA ITEM NO. 55-7.16
3 NOVEMBER 1970 THROUGH 2 FEBRUARY 1971
NASA CONTRACT NO. NAS1-6666

Document No. AP-71-7185

Number of pages 85

Original date 18 March 1971

Prepared by Engineering Staff

Edited by L. F. Jilly

Approved by E N Harris

Edward N. Harris
HRE Program Manager

Revision	Date	Pages Affected (Revised, Added, Eliminated)

FOREWORD

This interim technical data report is submitted to the NASA Langley Research Center by the AiResearch Manufacturing Company, Los Angeles, California. The document was prepared in accordance with the guidelines established by paragraph 5.7.3.2.2 of NASA Statement of Work L-4947-B (Revised).

Interim technical data reports are generated on a quarterly basis for major program tasks under the Hypersonic Research Engine Project. Upon completion of a given task effort, a final technical data report will be submitted.

The document in hand presents a detailed technical discussion of the structures and cooling development for the period of 3 November 1970 through 2 February 1971.

ACKNOWLEDGEMENTS

Acknowledgements for the completion of this document are herewith extended to the following contributors:

Development:	O. A. Buchmann C. M. Lee
Heat Transfer Analyses:	A. A. Vuigner C. F. Young
Stress Analyses:	W. G. Flieder

CONTENTS

ILLUSTRATIONS

ILLUSTRATIONS (Continued)

TABLES

1. SUMMARY OF STATUS

Testing of the Structures Assembly Model (SAM) continued throughout the reporting period at the NASA Langley 8-Foot High-Temperature Structures Tunnel. A total of 30 test runs have been completed, involving 38 loading cycles for the SAM. Fuel injection was used during 27 of the cycles. That portion of the program specifically aimed at thermal-cycling evaluation was completed.

For these runs, tunnel total conditions ranged to 2200 psia and 3000^{0}R. The tunnel nozzle is fixed and produces Mach numbers near 7 at the test conditions. The coolant for all runs was ambient-temperature hydrogen.

The condition of the SAM following these runs was satisfactory. Isolated leaks occurred at joints in the cooled structure, but they have not affected operation or resulted in local areas of overheating. Three punctures in the leading edge, caused by foreign object damage, were present during most of the runs; however, they showed no signs of propagation or distress due to overheating.

Testing will continue with runs at higher total pressures and temperatures than those run to date. Cryogenic hydrogen will be used as the coolant to accommodate the higher heat loads associated with these conditions.

2. PROBLEM STATEMENT

The objective of the structures and cooling development program is to analyze, design, and fabricate the regeneratively cooled surfaces and their associated structures and to verify the performance of these surfaces and structures at conditions that simulate the operating conditions expected in the flight test engine.

The Hypersonic Research Engine requires regenerative cooling on all surfaces that contact the engine airstream. The use of ablative coating on the engine aerodynamic surfaces is barred by the Statement of Work to minimize extraneous effects on engine performance. No such restriction is imposed on the engine cowl; therefore, ablative protection is acceptable for this component.

The characteristic design problem in regeneratively cooled structures for this type of application is associated with the large heat fluxes encountered over major portions of the engine surfaces. These heat fluxes range from values of approximately 10 Btu/sec-ft^2 to 1800 Btu/sec-ft^2 on the stagnation line of the support strut leading edge. The conservation of fuel requires that these heat fluxes be accommodated at temperature differences across the regeneratively cooled surfaces which range up to approximately 800^{0}F in flat surfaces and 1200^{0}F in leading-edge areas. These temperature differences in turn, result in strains that cause plastic deformation of the hot surfaces. Design, therefore, is governed by low-cycle fatigue conditions. Uncertainties associated with the prediction of low-cycle fatigue performance have led to heavy emphasis, in the experimental portion of the program, on the evaluation of the low-cycle fatigue performance of the engine components.

The general performance objectives set for the cooled structures are as follows:

Design life - 10 hr of hot operation of which 3 hr are to be taken at Mach 7 to 8 flight conditions

Cycle life - 100 cycles, at conditions which produce the highest plastic strain

3. TOPICAL BACKGROUND

The cooled structures, which were designed, fabricated, and tested as part of this task, and the associated connecting structures constitute the basic structural elements of the engine. The cooled surfaces of these structures form the aerodynamic surfaces of the engine, as shown in Figure 3.0-1.

3.1 GENERAL DESIGN ACTIVITIES

The original program definition incorporated installation and testing of the engine on the X-15A-2 airplane and the design guidelines were predicated on this. Subsequently, the program was reoriented to specify the fabrication of a Structures Assembly Model (SAM) engine and its testing in the NASA Langley 8-Foot High Temperature Structures Tunnel.

The regeneratively cooled surfaces were designed and fabricated to minimize engine performance losses. In addition to providing the basic contours, the cooled surfaces were fabricated and assembled in a way that avoided discontinuities; leading edges used the minimum radius compatible with reliable structural design.

Because of the research nature of the HRE program, temperatures and pressures are being measured throughout the engine. Consequently, the engine structures had to accommodate static pressure taps and metal temperature thermocouples.

The total amount of fuel available to the engine in flight and for cooling of its structure had to be limited to the storage capabilities of the aircraft to which it was to be attached. Consequently, in cooling the structure, fuel usage in excess of combustion requirements had to be minimized. To accomplish this goal, the cooled surfaces had to function at maximum metal temperatures and temperature differences compatible with sound structural design.

Engine internal structures and plumbing were designed to allow space for installing fuel system components, engine controls, instrumentation transducers, and signal conditioning equipment. Because of operating limitations, electronic equipment was installed in locations having the least severe environment.

To permit the engine to operate over the flight Mach number range from 3 to 8, the inlet spike had to be translated to various positions. To conserve coolant prior to and after engine operation, the inlet spike was translated to a position nearly in contact with the outerbody leading edge. Consequently, it was necessary to have a spike actuation system capable of the desired positioning accuracy, with control provided by the control system computer.

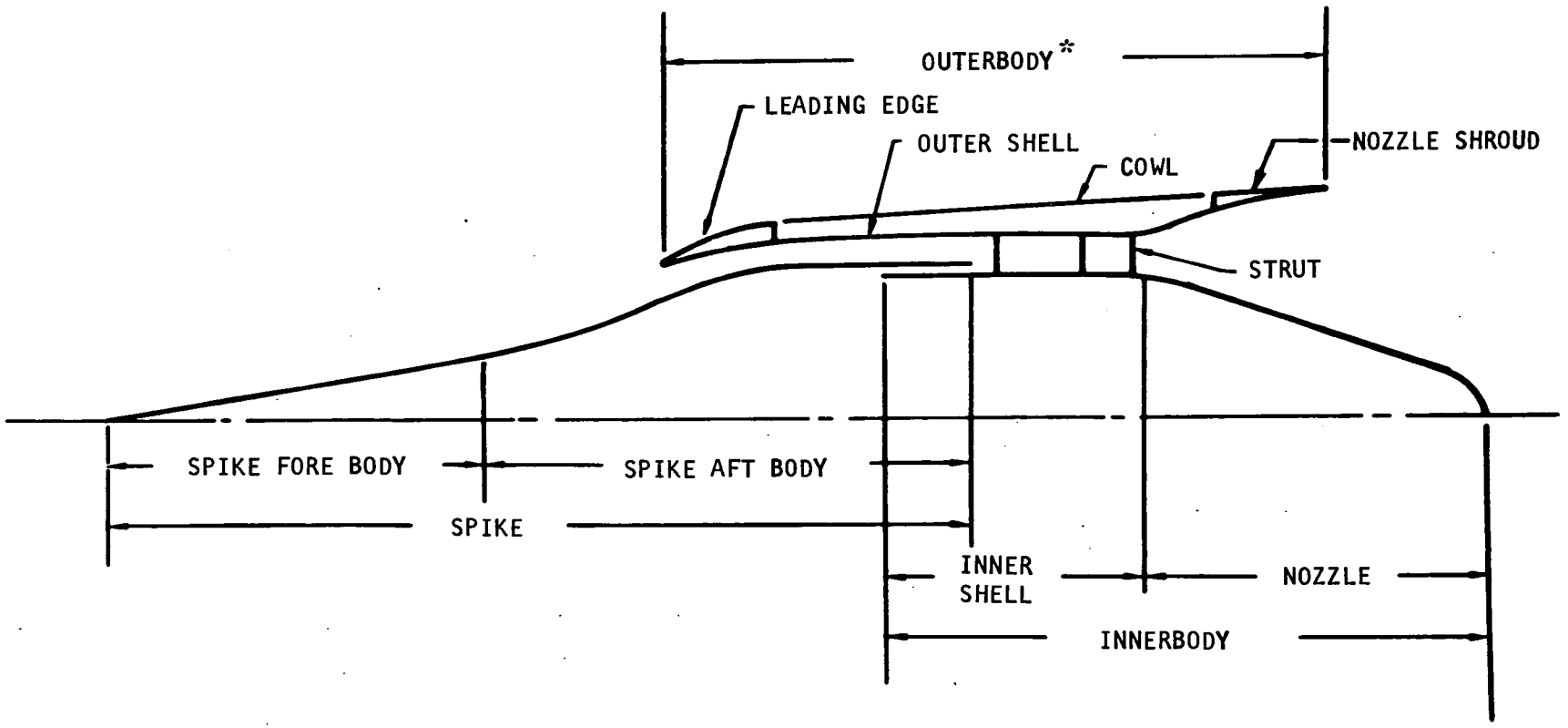

*OUTERBODY = LEADING EDGE + OUTER SHELL + NOZZLE SHROUD + COWL

A-30504

Figure 70-1. Cooled Structures Nomenclature

Engine fuel pressurization was to be provided by a hydrogen turbopump. Therefore, the total pressure drop in the regeneratively cooled surfaces, manifolds, and associated plumbing had to be compatible with the pressure output of the turbopump.

In addition to control of temperatures and temperature differences, the integrity of the coolant structures required that the flow routes within the engine be matched in such a way as to minimize temperature differences at axial stations for innerbody and outerbody surfaces. This was to minimize distortion of the engine internal passages. Axial temperature discontinuities as produced, for example, by the termination of two flow routes that differ greatly in temperature at the same station, were objectionable because of the severe thermal strains that would have resulted.

Measurement of engine internal thrust during operation was required. Consequently, external loads (drag and lift) that were transmitted directly to the thrust measuring device had to be minimized. Specifically, the engine cowl has drag loads that are of the same order of magnitude as the engine thrust. Mounting of the cowl in such a way as to minimize this external drag load, and thus the uncertainties in calculation of thrust, was therefore required.

A basic engine design requirement was that malfunction of the engine in flight would not endanger the safety of the aircraft to which it was to be attached or the life of its pilot. Therefore, provision had to be made to jettison the engine. Because of probable hydrogen leakage to the engine cavities, the innerbody engine cavity had to be either inerted or capable of containing an explosive mixture of hot hydrogen and air. The engine cavity was vented to near-nozzle base pressure to minimize the pressure resulting from hydrogen-air combustion and the structure designed to sustain the resulting loads. During ground checkout, the engine cavity was to be inerted with nitrogen.

The weight of cooled structures, inlet spike actuation system internal supporting structures, and plumbing was most of the total engine weight. Although optimization of the structures and structural components for minimum weight was not an objective, the specified weight limitation required careful consideration of structural weight.

3.2 OPERATIONAL BOUNDARIES

3.2.1 General Design Ground Rules

The maximum dynamic pressure specified for the current phase of the program is 2000 psfa. This compares with the specified dynamic pressure of 2500 psfa, specified for the HRE Phase I program. Consequently, the minimum altitude at Mach 8, during which cooling must be provided, is 85,000 ft, as compared to the Phase I minimum altitude of 81,000 ft. The minimum design altitude for the current program is 88,000 ft. The increased altitude results in a reduction of heat flux throughout the engine, but this reduction is offset in part by an increase in engine contraction ratio from 10 in Phase I to 14.6 in Phase IIA. In summary, the operating envelope for the engine is as follows:

Engine Structural Design - With engine either lit or not lit, dynamic pressure (q) = 2000 psfa

Engine Cooling Design

Normal design, engine lit: q = 1750 psfa, h = 88,000 ft minimum

Emergency design, engine lit: q = 2000 psfa h = 85,000 ft minimum

For the emergency design, engine lit conditions, all of the pump output pressure was to be available for coolant pressure drop. The dump valve was to open and fuel injection valves close as the aircraft approached these conditions from the normal operating line.

3.2.2 Engine Operating Cycles

A qualitative definition of the engine operating cycles was formed for the purpose of providing a basis for analyzing heat transfer transients evaluating the structural effect of transient temperature differences, establishing general control requirements and typical environmental conditions, and for defining acceptable operating cycles. The types of missions or conditions the engine must survive were as follows:

Case I - Constant M, with aircraft power on, at a constant high q

Case II - Constant M, with aircraft power off, aircraft diving

Case III - Variable M, expected to involve a change in M of 0.5 during 20-sec engine operating cycle

Case IV - Subsonic-supersonic combustion transition at M = 6

Case V - Inlet unstart, with shock expelled

Figure 3.2-1 is a qualitative representation of the critical cases. The common features, typical for all simulated missions, are numbered on the figure and are as follows:

1. Launch to M = 3+, during which the engine structure was assumed to go from a soak at -65°F to a soak at 1140°F. No cooling was required. At the end of this period, the helium purge was performed and coolant flow started through all portions of the cooled structure.

2. Approach to test Mach number, inlet closed (leakage flow only), during which coolant flow was increased to maintain maximum structure temperature (cold surface) at 1140°F.

3. Time for retraction of inlet spike to desired position. The solid lines assume programmed cooling flow; the dashed line assumes controlled cooling flow based on temperature sensing. The approach selected was a function of control system response and actuating system response. Controlled cooling is preferred.

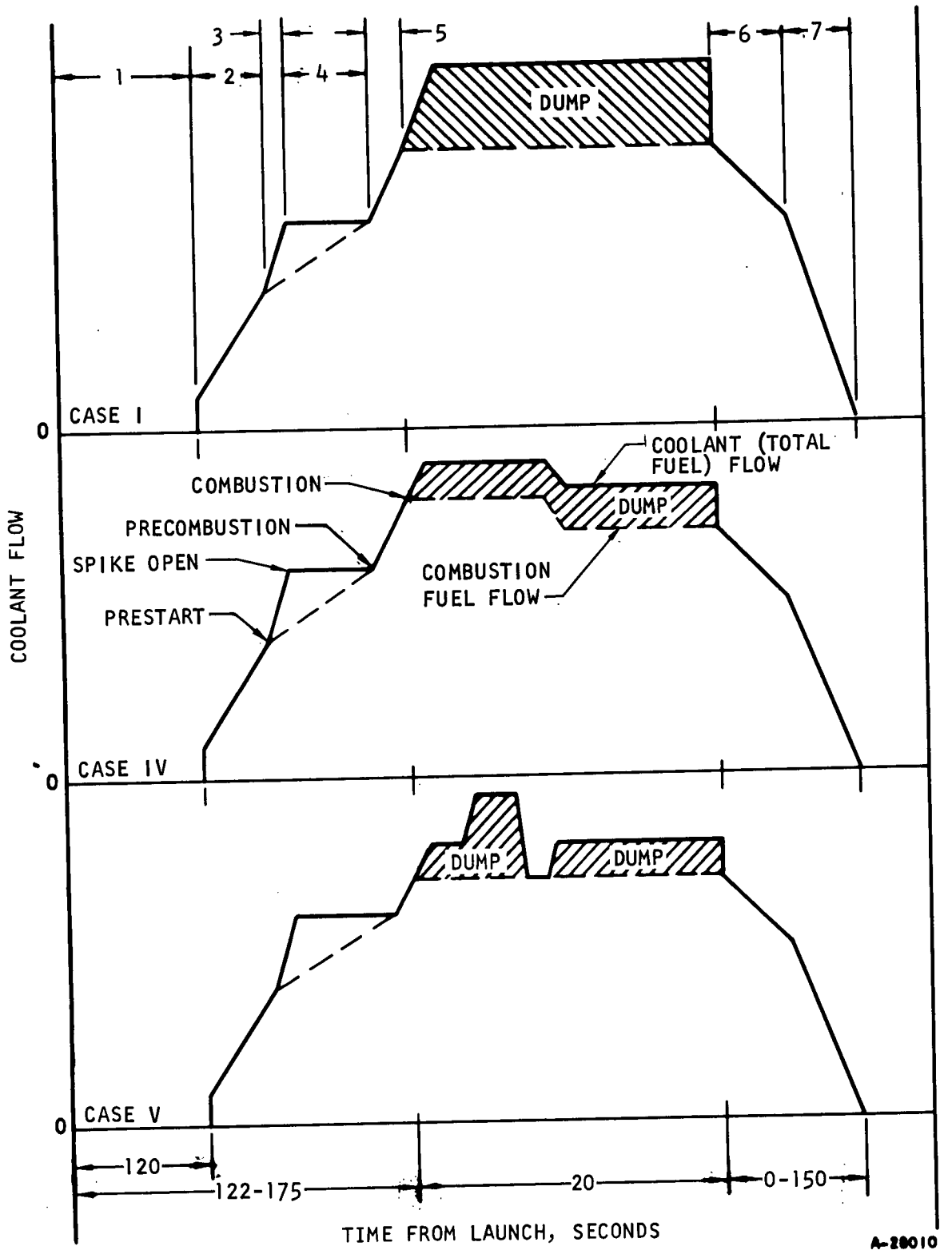

Figure 3.2-1. Typical Engine Operating Cycles

4. Inlet spike in starting position, full airflow through the engine, no combustion.

5. Programmed increase in cooling flow to starting combustion equivalence ratio (ϕ). This ϕ was less than the test ϕ. Combustion ϕ was to ramp to test ϕ (not shown).

6. Combustion terminated and inlet spike being extended to closed position.

7. Inlet closed (leakage flow only), deceleration to M = 4 +, with coolant flow decreased to maintain maximum structure temperature at 1140°F. Helium purge.

As combustion starts, the cooling ϕ had to be controlled to accommodate increasing heat fluxes. The variations among missions occurring during the combustion phase were as follows:

Case I - Shown in Figure 3.2-1. Cooling ϕ was in excess of combustion ϕ. Combustion ϕ ramped at beginning and end of test. Ramps of 5-sec duration to and from ϕ = 1 may be assumed at beginning and end of test.

Case II - Not shown. Represents a gradual change in conditions shown for Case I and involved less severe transients. Was not considered a design point.

Case III - Same comments as Case II, but may become a design point at lower Mach numbers because of potential for increased test time and wider Mach number range.

Case IV - Shown in Figure 3.2-1. Involved a near-step change in gas-side engine conditions during test run.

Case V - Shown in Figure 3.2-1. The general rise in pressure would be expected to cause a step-change type increase in heat flux. Spike would extend and close, then retract to operating position for second attempt at starting. At this point, either normal operation or a second unstart is possible.

4. OVERALL APPROACH

The diverse requirements imposed on the cooled structures required iteration of the cooled structural design with (1) the engine aerodynamic design; (2) the instrumentation, control, and fuel subsystems designs; and (3) the airplane interface design. Internal constraints on cooled structural design were imposed by the close coordination required in thermal design, structural design, mechanical design, and manufacturing. It was generally not possible to treat any one of these areas independently of the others. During Phase I of the program, the basic design concepts for the engine were defined and were basically feasible in terms of the contraints imposed on the design. These concepts and the design data generated during Phase I were used as the starting point for design of the Phase IIA cooled structures. Component layout drawings of acceptable mechanical design and with acceptable manufacturing features formed the initial step in the iteration. These layout drawings were evaluated to establish the required thermal and structural design features. Based on these inputs, layout drawings were revised to incorporate the required features, followed by substantiation of thermal and structural performance of the revised design.

Although the Phase I design was used as the starting point of Phase IIA cooled structure design, each of the components was reviewed with the objective of simplification in terms of mechanical design and manufacturing features. The interfaces between two or more components, in particular, were reevaluated. The interfaces included engine-to-support mounting, outer shell-to-innerbody mounting by means of the support struts, nozzle-to-inner-shell assembly, inlet spike-to-innerbody assembly, inlet spike actuator-to-inlet spike and innerbody mounting, leading edge-to-outer shell mounting, and cowl-to-outer shell support.

The general approach to cooled structures development places heavy emphasis on fabrication and testing of the full-scale components. A limited number of types of cooled structural elements and models were fabricated and tested to evaluate the problems which are basic to the overall engine design, or which were sufficiently localized in nature to permit use of subscale evaluation. All significant manufacturing development and evaluation was accomplished using the full-scale components. The nature of the required manufacturing operations for the components was such that use of subscale components would be expected to lead to only limited information on the adequacy of manufacturing techniques and processes.

4.1 THERMAL DESIGN

The overall thermal design approach was by analyses based on experimental data obtained from tests on similar geometric configurations and heat transfer situations. These experiment-based analyses, in turn, were verified by experiments where the geometry or fluid conditions, or both, were like those existing for the flight engine.

Where the discrepancy between calculated and experimental heat flux values was large, steps were taken to improve the analytical techniques so that the correlation between calculated and experimental results could be improved.

The basic goals of all thermal analyses and designs were (1) limiting temperature and temperature differences to structurally acceptable values, while keeping hydrogen cooling flow equal to or less than hydrogen flow required for combustion, and (2) at the same time maintaining hydrogen pressure drop compatible with cooling jacket pressure containment and pump outlet pressure capabilities. The limiting values used were (1) a maximum gas-side metal temperature of 1700°F (2160°R), (2) a maximum primary structure temperature of 1140°F (1600°R), and (3) a hydrogen pump outlet pressure of 1100 psia.

The thermal design procedure involved separate calculation of aerodynamic heating and cooling jacket performance. The aerodynamic heating conditions were calculated (as during Phase I) primarily by use of the computer program H1940. Special aerodynamic heating conditions, such as shock wave/boundary layer interaction, were computed separately. Cooling jacket fin performance was calculated (as in Phase I) by use of computer program H1930. Special conditions, such as pressure and flow distributions for inlet, outlets, and bolted flange/manifolds, required separate calculations. Verification of selected aerodynamic and cooling jacket heat transfer and pressure drop calculations was accomplished by actual tests.

4.2 STRUCTURAL DESIGN

The structural design approach utilized a combination of analytical and experimental methods. Experimental verification of detailed parts, such as short-term burst, creep-rupture, and thermal fatigue tests on sandwich plate-fin elements, were employed wherever necessary.

The bulk of the HRE structures consists of ring-stiffened orthotropic shell structures of variable thicknesses and contours. The ring stiffeners are also used for coolant flow manifolding and fuel injection rings for the engine combustor section. The structural loadings will produce axisymmetric and asymmetric forces and moments due to static normal pressures, acceleration, vibrational inputs and aerodynamic flutter and buffeting effects.

Fully operational computer solutions are available to analyze axisymmetric isotropic thin shells of variable thicknesses and contours for stresses due to axisymmetric loads and temperature profiles. In addition, the isotropic shell analysis had been extended to treat orthotropic cylindrical shells with axisymmetric loads. Two MIT finite difference nodal circle solutions (SABOR III

and DASHER I), which have been adapted for use on the AiResearch computer system (IBM-360/50), are available for use.

The SABOR III program is applicable for axisymmetric isotropic shells (local departures from ideal isotropy can be treated) that may be subjected to nonsymmetrical static forces. The SABOR III program may also be used to obtain the stiffness and mass matrixes for direct input into the DASHER I program to obtain dynamic response.

It would have required an extensive programming effort to modify the SABOR III and DASHER I programs to treat accurately many of the problems that were encountered in the HRE. Rather than attempt this approach, a further survey of existing shell programs was carried out, and it was determined that an extremely applicable program had been developed under the auspices of the Analysis Group of the Theoretical Mechanics Branch, Structures Division of the Wright Patterson Air Force Base, Dayton, Ohio. This program is based upon the very recent improvement in matrix shell solutions generated by A. Kalnins (Department of Mechanics, Lehigh University). It solves the general axisymmetric orthotropic thin shell problem for symmetric and nonsymmetric loads due to static as well as dynamic inputs. The program has been successfully adapted for use on the AiResearch computer system. Although the program has been debugged, the final report describing the usability limitations, and methods of data input has not been completed, and will not be released by the Wright Patterson Air Force Base for at least twelve months. Until a program of this magnitude has been completely checked out by trying numerous test cases, a note of caution must be exercised regarding its capabilities. Another important point is the fact that the problem inputs and the data reduction of the outputs require considerable effort on the part of the user. The existence of the program also does not eliminate or substantially reduce the work needed to generate a sound design; however, it is the objective of careful analysis to discover design inadequacies that would otherwise not be recognized.

The eventual objective of the test program is to verify the actual performance capabilities of the structures as fabricated. Although it will not be possible to predict analytically the influence of realistic fabrication restrictions and limitations on the end product, the initial analysis will identify the serious design problem areas. Results of the test program will be used to assess the extent of the changes required to achieve the structural integrity goals.

4.3 MECHANICAL DESIGN

The guidelines used in mechanical design of the cooled structures components and assembly of the components into the engine required the use of known materials and joining techniques. Standard fasteners and seals were used to the greatest extent possible. Design for brazing was aimed at minimizing the total number of braze cycles to which a given part must be subjected. In some cases, this was done by redesigning the parts to allow use of prebrazed subassemblies, substitution of machined or welded subassemblies, or substitution of bolted interfaces for brazed or welded interfaces. Also, as a general rule, all welding into or close to braze joints was avoided, although

in certain cases, such a procedure was acceptable.

The mechanical design effort was supported by experimental verification in selected areas. In particular, selected configurations that presented analytical problems and raised questions as to manufacturing feasibility were fabricated and tested on a subscale basis. The purpose of such tests was to provide design data and guidance for possible design revision. Tests, which were in support of mechanical design, rather than thermal or structural design, included the following:

Test specimen to evaluate feasibility of bolting the nozzle flange manifold to the inner shell through the removable nozzle cap

Fabrication of a section of the inlet spike near the spike tip to help resolve questions regarding the best manufacturing approach, and hence, the best design for this portion of the inlet spike

Fabrication of a straight section of the bolted nozzle manifold to verify both the manufacturing aspects and structural integrity of the design solution

Fabrication of flat panels using the various instrumentation and fuel injector fittings that penetrate the regeneratively cooled surfaces to verify manufacturing feasibility and structural integrity of the design. Tests results were used to select the final configuration used in the engine.

4.4 MANUFACTURING

The manufacturing approach used on this program had two aspects: (1) that dealing with the approach to development of manufacturing techniques and processes, and (2) that dealing with the specific manufacturing processes planned for use.

4.4.1 Development Approach

The development of the manufacturing techniques and processes relied primarily on full-scale components. Except where isolated problems required solution or basic data was needed, the use of subscale components represented a duplication of development effort. The compound forming of the shell face sheets in half-scale, for example, resulted in working with radii of curvature which were half those encountered in the full-scale part. Use of lighter-gage material to facilitate forming, on the other hand, was impractical. In addition, the size of the full-scale tooling, the machines required to use this tooling, and the unique problems associated with the forming of large thin-wall shells could not be duplicated in half-scale. As a result, a half-scale compound-curved model of the isentropic surface of the inlet spike was the only subscale component on which fabrication development work was done. This part was used to establish forming characteristics, evaluate electrohydraulic forming parameters, and investigate brazing problems.

4.4.2 Fabrication Approach

The most critical area of cooled structures fabrication was in the cooled-surface shell face sheets. The starting point for these shells was rolled-and-welded-cone sections. The rolled-and-welded cones were bulge-formed, then final-sized, using electrohydraulic forming. The weld seam was not considered structurally objectionable and the approach involved fewer steps than were required for other techniques.

To ensure adequate braze fitup, forming accuracy for the shells had to be high. Specifically, it was expected that the clearance between shells must be maintained within a tolerance of approximately ±0.001 in. Given this accuracy, the brazing of the fins between the face shape still required special attention. To ensure sound braze joints, pressure had to be exerted on the shells in such a way as to provide a crushing load on the fins. The methods used for providing this braze fixturing load included the following, as a function of the component being brazed:

> Graphite fixtures, with an external piece containing the assembly and an internal piece using expanding segments to exert pressure.
>
> Steel bags placed inside the shell and pressurized to a level sufficient to deform the shell with which the bag is in contact. Containment on the external face sheet may or may not be required with this approach.

Integrity of the shell joining was experimentally evaluated, and adjustments in shell-forming tools and brazing procedures and fixtures made to correct problems that appeared.

4.4.3 Nondestructive Testing

The critical area in fabrication of the full-scale components involved the shells themselves, as discussed in the two previous paragraphs. For structural integrity of the shells, only very limited areas of unbrazed joint areas were tolerable. These joints were detectable by proof-pressure testing at sufficiently high pressure levels. Only in exceptional cases, however, would a defect that was revealed by proof-pressure test be repairable. In general, a nondestructive test capable of revealing braze voids is preferable and offers better opportunity for subsequent repair. The two techniques available were radiographic inspection of the entire shell surface and the use of stress-sensitive lacquer on the face sheets. These methods showed a braze void; that is, an unbonded joint. Weak joints were not discernable as such. In general, however, the existence of a brazed joint was reasonable assurance that adequate joint strength could be achieved.

The repair for unbonded joints in the shells generally consisted of recycling of the complete shell to a slightly higher temperature than used during the first braze cycle. In this way, remelt and flow of the braze alloy was obtained with the objective of filling the void. Orientation of the shell in the brazing furnace was used to assist the process.

5. ANALYTICAL DESIGN

(No reportable activity in this Section during the reporting period).

6. DESIGN EFFORT

(No reportable activity in this Section during the reporting period).

7. MANUFACTURING

During the reporting period an investigation was conducted into various methods of sealing holes in the hot skin of the engine. The investigation included determination of the most practical techniques for removal of oxides and cleaning of the surfaces and for the joining of miniature patches over the holes.

7.1 COWL LEADING EDGE REPAIR

In the course of wind tunnel testing, the forward end of the cowl leading edge assembly has sustained damage from the impact of particles in the gas stream. This damage has been in the form of small dents, gouges, and perforations in the surface of the hot skin, in the area between the stagnation point and the doubler, as illustrated in Figures 7.1-1 and 7.1-2. Perforations of the hot skin occurred in three places. One of these was a hole approximately 0.045 in. x 0.065 in., as shown in Figure 7.1-1. The leakage of coolant through these holes could be tolerated during testing. The possibility of propagation of damage due to thermal cycling of the highly stressed areas around the holes led to the investigation of techniques for sealing the holes. Actual repair would only be accomplished if essential to continuation of testing. This has not been the case to date.

7.2 APPROACH

The hole geometry and locations fall into two categories; (1) a tiny hole and denting at the stagnation line (Figure 7.1-2),and (2) holes in the relatively flat surfaces aft of the stagnation line (Figure 7.1-1). The repair at the stagnation line, because of the size of the hole, appeared possible by Gas Tungsten Arc (GTA) brazing without the need to fit filler plugs or patches. The repair of the holes in the flat surfaces was accomplished by the use of small patches or plugs of the parent metal joined to the skin. Figure 7.2-1 illustrates the geometry of the patch that was used.

7.2.1 Cleaning

The primary constraints on the cleaning technique were the requirement that it be completely portable, and that it do nothing to contaminate the fins inside the holes. Portability was required to permit repair of the SAM while installed in the wind tunnel test section.

An initial attempt to remove the surface oxidation was made using stylus-type electrolytic cleaning. This proved to be unsatisfactory because of extremely deep localized surface pitting.

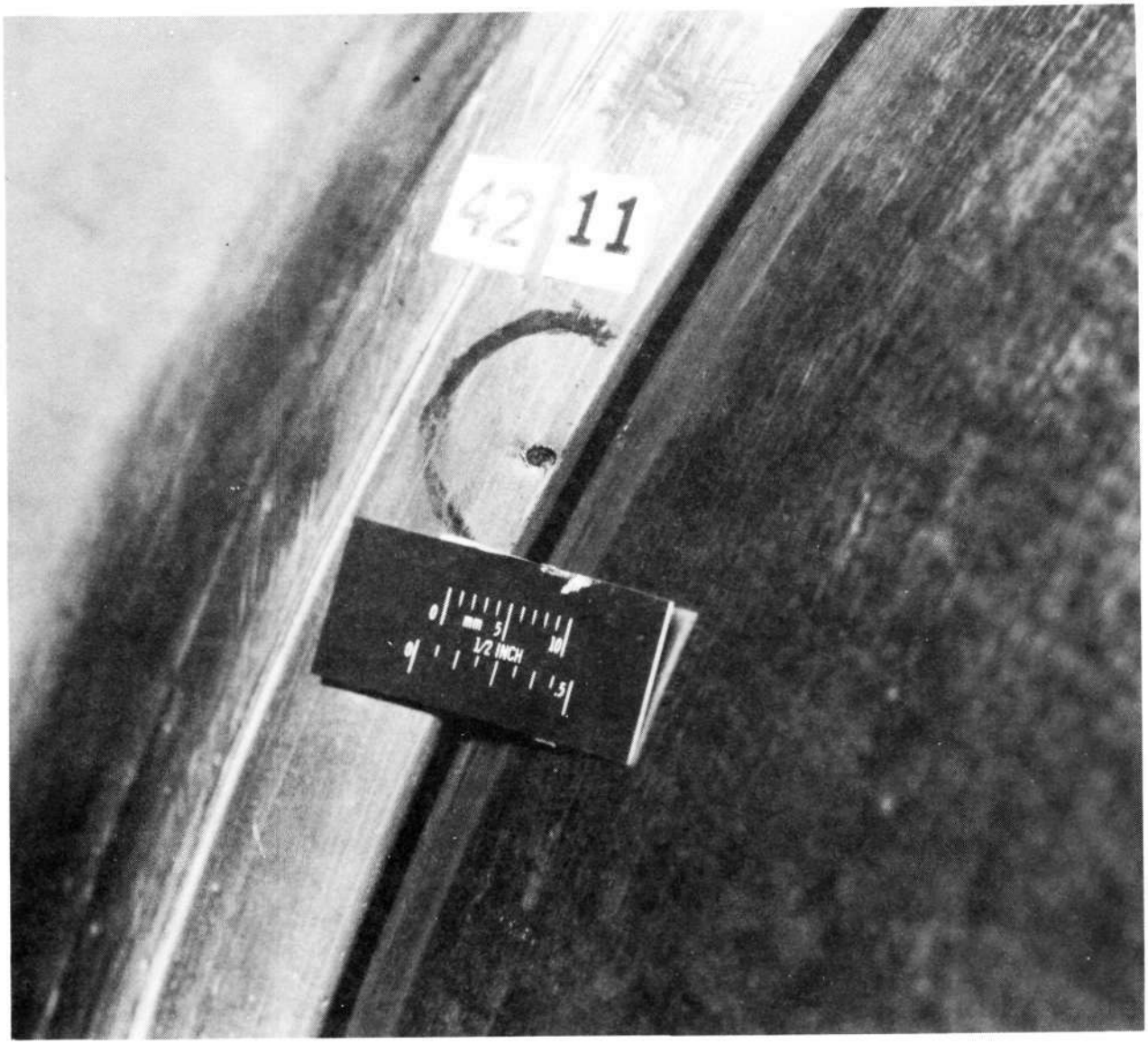

F-13062

Figure 7.1-1. SAM Leading Edge Skin Damage - Hole in Flat Outer Surface

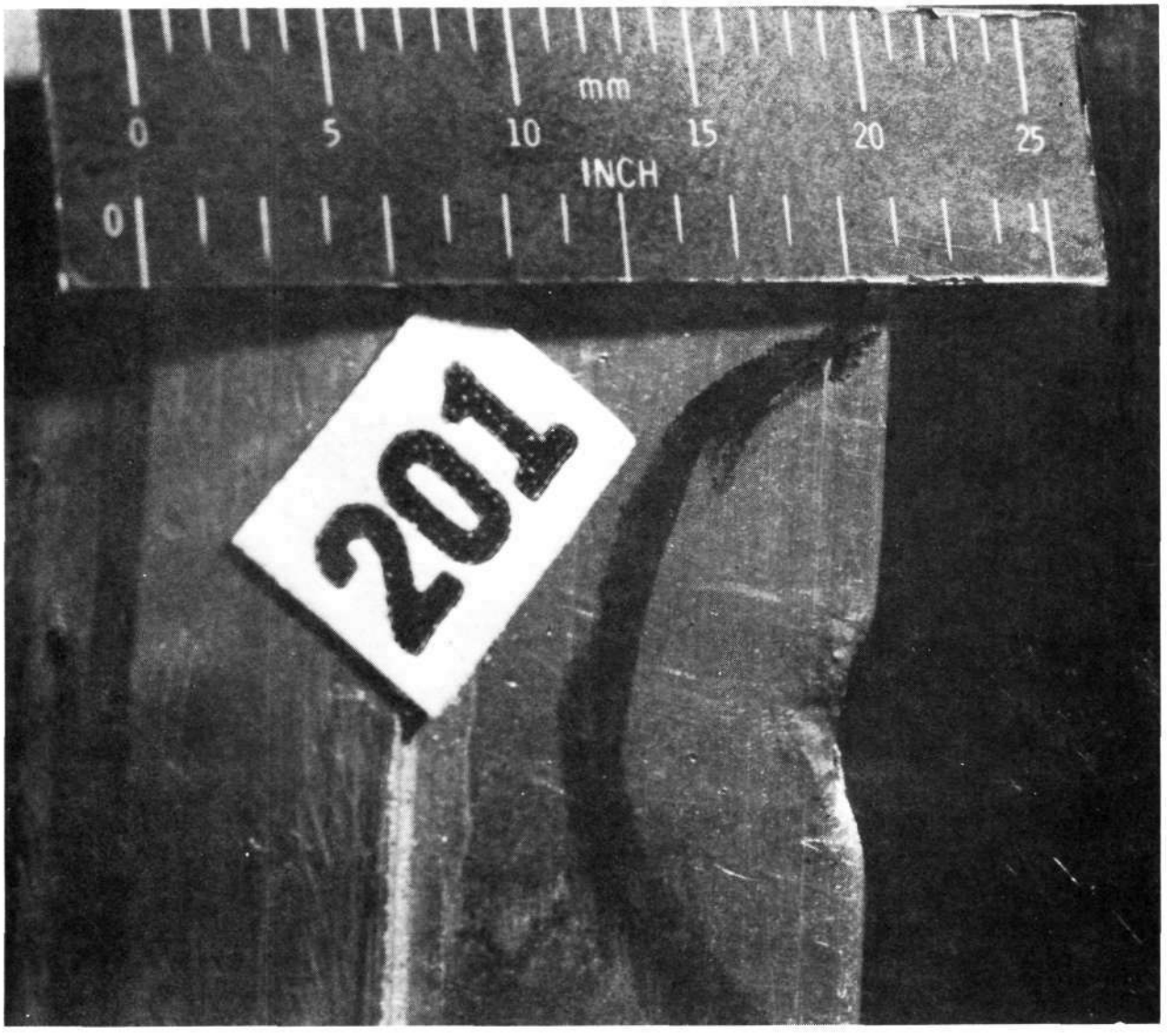

F-13061

Figure 7.1-2. SAM Leading Edge Tip Damage - Dent and Leak Caused by Foreign Object Impingement

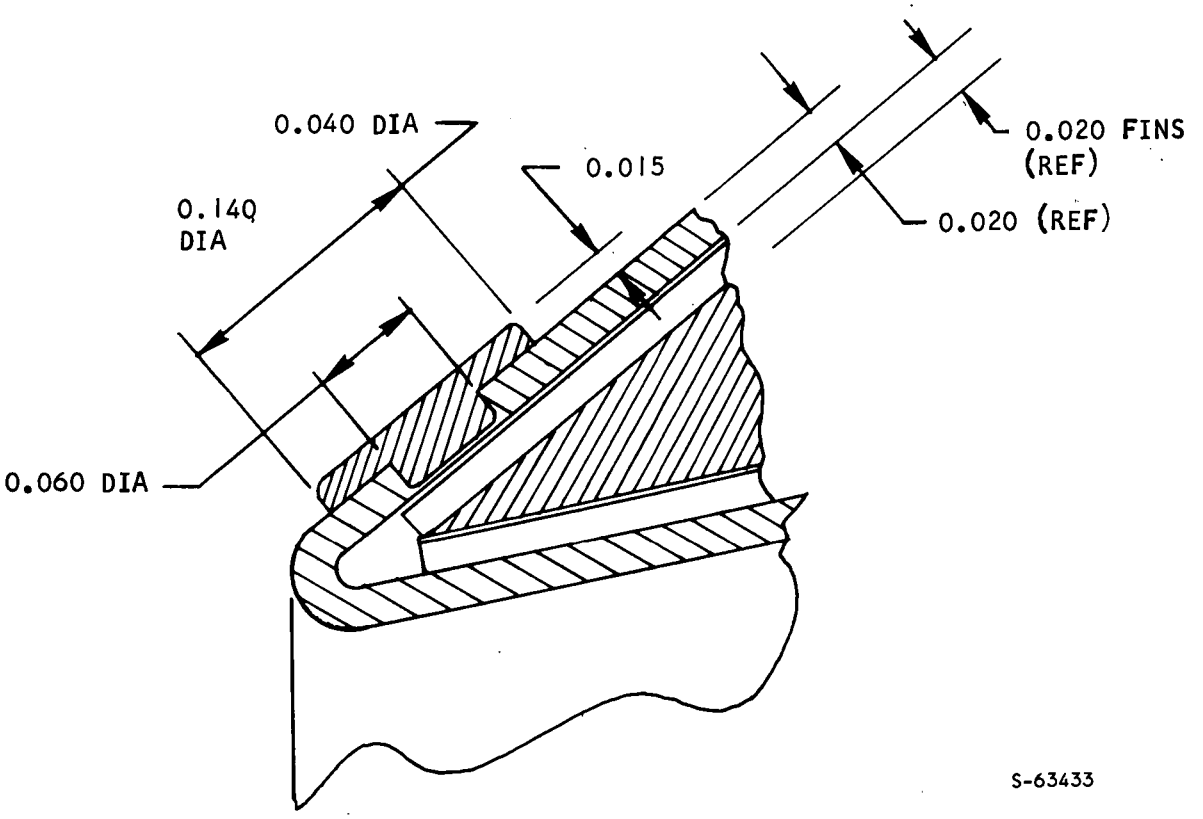

NOTE: ALL DIMENSIONS ARE IN INCHES

Figure 7.2-1. Flat Surface Patch Geometry

Abrasive cleaning using S. S. White "Airbrasive" equipment and silicon carbide grit was found to be satisfactory for oxide removal. The equipment is portable, requiring only a supply of compressed air.

A third technique, however, was found to be equally effective in removing the oxides without necessitating specialized equipment. It consisted of the mechanical breaking up of the oxide with No. 280 grit, silicon carbide paper followed by a "sweeping" of the surface with a GTA electrode using a reverse-polarity high-frequency arc.

7.2.2 Repair

The investigation of repair techniques consisted of a review of the various options and the elimination of all but the three most promising for each of the two types of holes. Sample repairs were made on holes in flat panels and the repair integrity was evaluated by pressure testing and metallography. Following this activity, repairs were made to holes in portions of leading edge straight sections and evaluated by metallography.

The techniques selected for further activity were:

Leading Edge Flat Surfaces

(a) GTA Braze using Nioro Alloy

(b) Laser Braze using Nioro Alloy

(c) GTA Weld using Hastelloy W Alloy

Leading Edge Stagnation Line

(a) TIG Braze using Nioro Alloy

(b) Dallic Nickel Plating

(c) Laser Braze using Nioro Alloy

Three patches were GTA-brazed to a flat panel, varying the placement of Nioro braze alloy slightly from joint to joint. No significant visual difference could be observed. The panel was then connected to a hydraulic pressure-testing rig and pressurized to failure. This occurred at 6750 psig when the fins failed. The patched holes were then sectioned and examined; a typical joint appearance is shown in Figure 7.2-2. Good alloy flow and metallurgical bond with the patch and parent metal was observed. Patches were then GTA-brazed to leading edge straight sections, incorporating on these sections the reverse-polarity GTA electric cleaning technique referred to above. The appearance of one of these joints is shown in Figure 7.2-3. Somewhat less alloy flow is noted, but this is felt to be controllable by adjustment of electrode current.

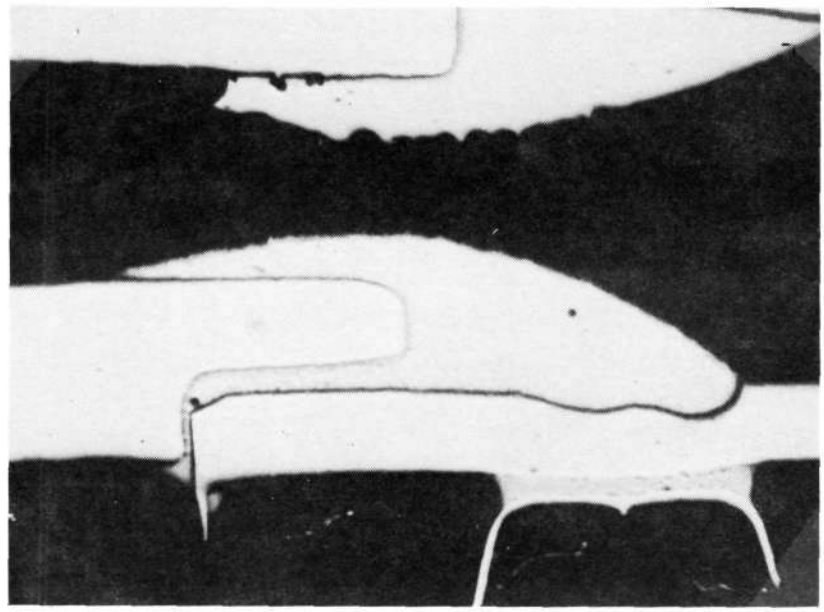

Figure 7.2-2. G.T.A. Braze Joint, Nickel-200 Patch in Hastelloy X Skin (Flat Panel), Nioro Braze Alloy (Mag 10X Approx)

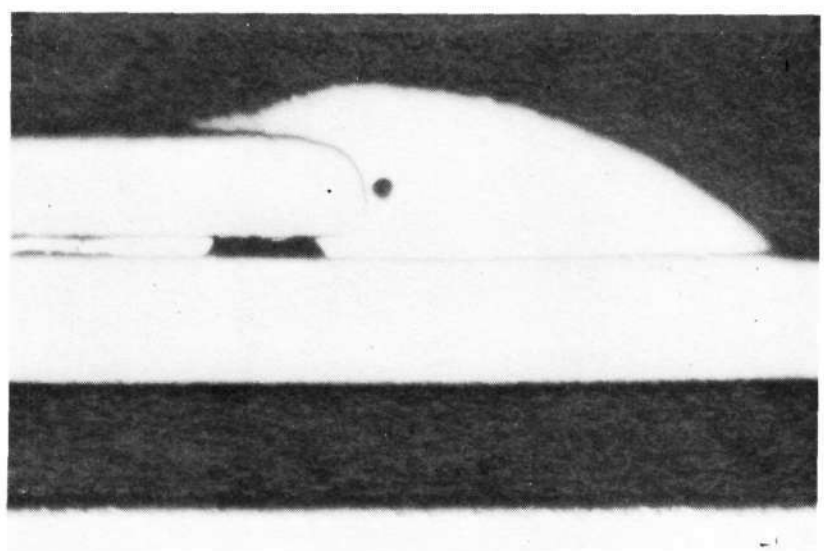

F-13059

Figure 7.2-3. G.T.A. Braze Joint, Nickel-200 Patch in Nickel-200 Skin (Leading Edge) Nioro Braze Alloy, G.T.A. Reverse-Polarity Cleaning

A series of patches were brazed to a flat panel using a laser beam as a heat source. The appearance of a typical joint is shown in Figure 7.2-4. The complete lack of alloy flow caused abandonment of this technique.

After the cleaning technique had been established, dents similar to that shown in Figure 7.1-2 were formed in the tip of a leading edge straight test section sample. The area was then cleaned using GTA reverse polarity, and Nioro braze alloy was flowed on the area. The technique proved to be relatively easy to control in terms of limiting the heated zone. Figure 7.2-5 shows a section through the bead produced.

7.3 RESULTS AND CONCLUSIONS

The investigations described above resulted in the production of sound repair joints in thin skins (0.015/0.020) that did not disturb the fin passages or create unacceptable protuberances in the outer surface. The only specialized equipment required includes a conventional GTA torch and a power supply with high-frequency ac capability and accurate control in the range of 2 to 18 amperes. Localized repair of the SAM in the wind tunnel test section is, therefore, considered possible with high confidence of success.

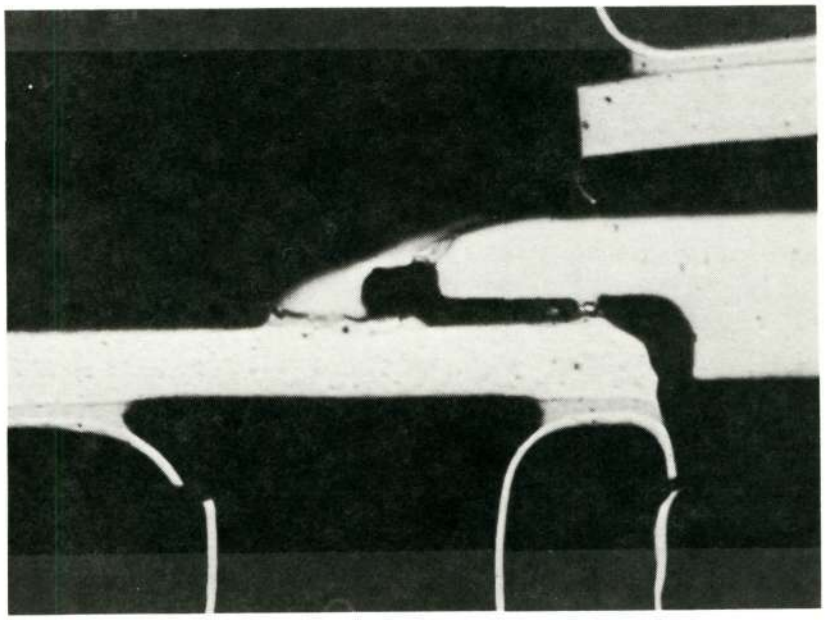

Figure 7.2-4. Laser Braze Joint, Nickel-200 Patch in Hastelloy X Skin (Flat Panel), Nioro Braze Alloy (Mag 10X Approx)

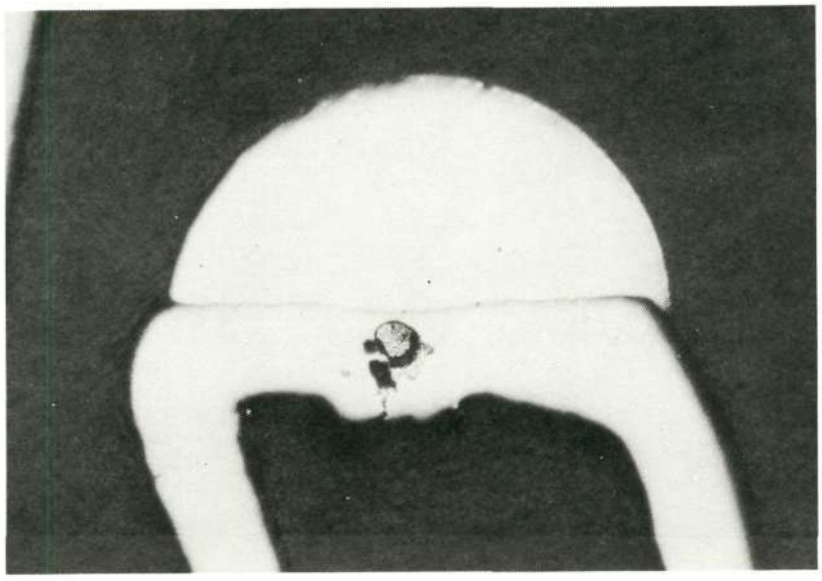

F-13060

Figure 7.2-5. G.T.A. Brazed Bead, Nickel-200 Leading Edge Tip, Nioro Braze Alloy, G.T.A. Reverse-Polarity Cleaning

8. TESTING

A total of 30 SAM thermal performance and cycling test runs have been performed to date (through Test 42, Run 36). The runs have been divided into two test groups; the first group, designated as Test 41, emphasizes the collection of aerodynamic and thermal performance data (through Test 41, Run 29). The second group, designated as Test 42, is aimed at the accumulation of thermal-structural data. Twenty-nine thermal cycles were performed in these latter test runs, most of them using hydrogen injection. Instrumentation hookups for the two test groups differed to reflect the test emphasis. A total of 40 cycles have been accumulated for all 30 test runs.

8.1 SUMMARY OF TESTS

A summary of the test conditions and operating parameters is presented in Table 8.1-1. Corresponding AiResearch run numbers as defined in Reference 8-1 are included in this table. Tunnel total pressures and temperatures ranged from 920 to 2200 psia and from 2500 to 3100°R, respectively. Model insertion times ranged from 13 to 68 seconds. Most test runs were performed with a spike retraction (from the fully closed, latched position) of approximately 2.9 inches; three runs were at 2.3 in. and one run was at 1.7 in. spike retraction. During two of the runs, the spike was not retracted. All positions gave a spike shock outside the leading edge (the shock-on-lip spike position is at approximately 3.9 in. of spike retraction at 1350 psia and 2700°R tunnel total conditions). Of the 30 test runs, 17 (all Test 42 runs except Runs 16 and 34) were performed with partial or full coolant-jacket hydrogen flow injected into the hot gas stream. Most of the thermal cycling (Test 42, Runs 17 to 36) was achieved by inserting the SAM into the tunnel gas stream twice during a test run, with an intermediate withdrawal into the tunnel pod. Three thermal cycles were performed for Test 42, Run 21.

8.1.1 Measured Data

Thermal performance tests (Test 41, Runs 5 to 29) were run for the purpose of collecting steady-state aerodynamic and thermal data on the hydrogen-cooled plate-fin surfaces of the model. The planned test procedure was to insert the model into the operating tunnel and retract the spike, insertion and retraction taking 4 to 5 seconds. The model was held in the tunnel up to 50 seconds. Steady-state aerodynamic conditions, as determined by wall static pressure measurements, were achieved in less than five seconds of run time for most locations (partial plugging of some of the static lines appreciably increased the response time). Steady-state thermal conditions, as determined by coolant outlet temperature histories, were achieved after about 30 seconds for the spike and leading edge flow routes. Steady-state thermal conditions were not achieved for the inner body, trailing edge, and strut flow routes for almost all

TABLE 8.1-1

SUMMARY OF HRE SAM STRUCTURAL AND COOLING TESTS

LRC			AiResearch Run No.	Tunnel Total		Time in Tunnel, sec	Spike Retraction, in.	H_2 Injection	Nom. Venturi H_2 Flow Rate, lb/sec	Max Outlet H_2 Temp, T101, °R	Max H_2 Heat Load, Btu/sec	Outerbody Outlet Manifold					Remarks
Test No.	Run No.	Cycle No.		Pressure, psia	Temp, °R							$\Sigma\Delta T$, °R	Max Hot Wall Temp, °R	$\Delta(\propto\Delta T)$	Damage Fraction	Accum. Damage	
41	5	1	2	975	2600	46	2.34	No	0.38	1025	650	660	1260	0.00535	0.0013	0.0013	
41	7	1	2	960	2600	32	2.30	No	0.19	1210	497	680	1680	0.00620	0.0031	0.0044	Automatic shutdown due to SAM over-temperature.
41	12	1	3	950	2500	13	2.88	No	0.29	850	337	661	1110	0.00520	0.0010	0.0054	
41	13	1	3	920	2500	42	2.89	No	0.23	1160	508	845	1370	0.00710	0.0041	0.0085	Foreign object damage (FOD) in 13 areas of leading edge.
41	16	1	5	1300	2600	42	2.89	No	0.35	1180	770	805	1360	0.00674	0.0034	0.0129	
41	17	1	5	1290	2700	49	2.89	No	0.35	1220	820	840	1420	0.00700	0.0040	0.0169	
41	20	1	7	1540	2700	45	2.86	No	0.31 - 0.44	1291	911	1122	1565	0.00952	0.0114	0.0283	Dent and leak at leading edge stagnation line due to FOD.
42	3	1	4	950	2600	39	2.85	Yes	0.24 - 0.33	1210	480	819	1380	0.00680	0.0035	0.0318	
42	11	1	6	1275	2700	44	2.89	Yes	0.25 - 0.47	1290	830	1207	1555	0.01020	0.0138	0.0456	0.045 x 0.065-in. hole in side of leading edge tip due to FOD.
42	12	1	8	1510	2800	41	2.89	Yes	0.25 - 0.40	1310	1100	1035	1510	0.00875	0.0086	0.0542	
41	26	1	30	2200	3100	16	1.70	No	0.31 - 0.47	1205	770	1215	1675	0.01037	0.0158	0.0700	Automatic shutdown caused by electrical noise.
41	27	1	30, 31	2200	3000	40	0.0	No	0.34 - 0.41	682	190	---	---	---	0	0.0700	No spike retraction. Control error. 0.010-in. dia hole in side of leading edge.
41	28	1	30, 31	2200	3000	22/8	2.33/2.87	No	0.37 - 0.51	1350	1380	1265	1550	0.01055	0.0151	0.0851	Two spike positions. Automatic shutdown due to methane alarm. Leak at nozzle-inner shell port seals; replaced these.
41	29	1	9	1380	2700	50	2.86	No	0.20 - 0.50	1310	690	1215	1570	0.01027	0.0142	0.0993	Leak at aft end of strut No. 5.
42	14	1	8	1530	2700	52	2.89	Yes	0.25 - 0.35	1410	800	1300	1637	0.01093	0.0177	0.1170	
42	16	1	10	1375	2700	7/6/6	0.0	No	0.38 - 0.42	680	---	130	708	---	0	0.1170	Four model insertions. No spike retraction. Determine minimum ejector pressure.
42	17	1	10	1360	2700	68	2.89	Yes	0.16 - 0.35	1320	690	1050	1384	0.00813	0.0079	0.1249	
42	19	1	11	1380	2700	21	2.89	Yes	0.24 - 0.31	1100	480	770	1390	0.00648	0.0030	0.1279	Leak at nozzle-inner shell port seals; replaced these with rubber O-rings.

TABLE 8.1-1 (Continued)

LRC			AiResearch Run No.	Tunnel Total		Time in Tunnel, sec	Spike Retraction, in.	H_2 Injection	Nom. Venturi H_2 Flow Rate, lb/sec	Max Outlet H_2 Temp, T101, °R	Max H_2 Heat Load, Btu/sec	Outerbody Outlet Manifold					Remarks
Test No.	Run No.	Cycle No.		Pressure, psia	Temp, °R							$\Sigma\Delta T$, °R	Max Hot Wall Temp, °R	$\Delta(\alpha\Delta T)$	Damage Fraction	Accum. Damage	
42	19	2	11	1380	2700	22	2.89	Yes	0.24 - 0.31	1200	560	715	1430	0.00627	0.0028	0.1307	
42	21	1	12	1380	2800	14	2.90	Yes	0.18 - 0.27	1080	300	1017	1500	0.00856	0.0080	0.1387	
42	21	2	12	1380	2800	14	2.89	Yes	0.18 - 0.27	1120	410	723	1364	0.00605	0.0022	0.1409	
42	21	3	12	1380	2800	15	2.89	Yes	0.18 - 0.27	1130	380	735	1378	0.00612	0.0024	0.1433	
42	22	1	13	1370	2700	19	2.89	Yes	0.25 - 0.43	1220	380	945	1636	0.00817	0.0077	0.1510	
42	22	2	13	1370	2700	20	2.88	Yes	0.20-0.22	1280	540	610	1506	0.00528	0.0015	0.1525	
42	24	1	14	1370	2700	24	2.89	Yes	0.19 - 0.22	1080	460	1010	1480	0.00842	0.0075	0.1600	Automatic shutdown due to methane alarm after one cycle.
42	25	1	15	1380	2700	14	2.90	Yes	0.13 - 0.18	1080	460	1020	1500	0.00850	0.0078	0.1678	Leak at forward end of strut No. 5
42	25	2	15	1380	2700	13	2.89	Yes	0.14 - 0.17	1090	270	820	1370	0.00682	0.0036	0.1714	
42	28	1	16	1370	2700	18	2.89	Yes	0.19 - 0.33	1216	450	1139	1576	0.00965	0.0120	0.1834	
42	28	2	16	1370	2700	15	2.89	Yes	0.16 - 0.21	1260	420	724	1490	0.00620	0.0027	0.1861	
42	29	1	17	1380	2700	19	2.89	Yes	0.20 - 0.30	1220	400	1122	1563	0.00940	0.0110	0.1971	
42	29	2	17	1380	2700	17	2.88	Yes	0.16 - 0.20	1290	410	810	1518	0.00720	0.0042	0.2013	
42	30	1	18	1380	2700	31	2.89	Yes	0.15 - 0.23	1320	510	1147	1560	0.00955	0.0115	0.2128	Leak at forward end of strut No. 2.
42	31	1	19	1380	2750	22	2.90	Yes	0.18 - 0.21	1160	360	935	1452	0.00760	0.0053	0.2181	
42	31	2	19	1380	2750	34	2.90	Yes	0.16 - 0.20	1320	400	841	1516	0.00710	0.0045	0.2236	
42	32	1	20	1380	2700	19	2.89	Yes	0.08 - 0.20	1150	360	1064	1498	0.00877	0.0086	0.2322	Leak at forward end of strut No. 3.
42	32	2	20	1380	2700	31	2.89	Yes	0.08 - 0.20	1310	450	870	1547	0.00636	0.0031	0.2353	
42	33	1	21	1380	2700	20	2.89	Yes	0.09 - 0.21	1150	400	905	1429	0.00713	0.0043	0.2396	
42	33	2	21	1380	2700	31	2.90	Yes	0.09 - 0.21	1310	460	921	1536	0.00768	0.0058	0.2454	
42	34	1	22	1390	2700	67	2.90	No	0.19 - 0.41	1300	720	1388	1573	0.01155	0.0198	0.2652	
42	36	1	23	1390	2700	59	2.89	Yes	0.14 - 0.23	1360	660	1183	1570	0.00980	0.0124	0.2776	Leak at aft end of inner shell.

thermal-performance and thermal-cycling tests. Measured metal temperatures on the spike and leading edge reached steady-state as soon as the coolant temperatures reached steady-state. Metal temperatures on the inner body and trailing edge responded to the hot gas heating as quickly as those on the spike and leading edge, but after the initial response, tracked the adjacent transient coolant temperature.

Thermal-cycling runs (Test 42, Runs 11 to 36) were performed for the purpose of accumulating low-cycle thermal fatigue performance data for the model. The model was inserted into the tunnel for 15 to 30 seconds and then withdrawn. For several tests the model was reinserted into the tunnel for an additional 15 to 30 seconds, after a 10- to 15-second dwell time in the pod. Hydrogen flow was maintained in the routes for this dwell period. The absolute sum of the maximum-positive and maximum-negative wall-to-structural ΔT for the outer body outlet manifold for each test run is indicated in Table 8.1-1. The calculation of the low cycle fatigue damage fraction (indicated in Table 8.1-1) is discussed in paragraph 8.3.3.

8.1.2 Observed Data

8.1.2.1 Metal Discoloration

Both Hastelloy X (used as face sheets for the regeneratively cooled shells) and nickel (used as the hot skin for the leading edge tip) show distinct surface discolorations as a function of temperature. In addition, surface preparation immediately prior to exposure strongly affects the appearance of the oxide films in certain temperature ranges. These phenomena were used to obtain estimates of hot skin temperatures in areas of high local heating where thermocouple instrumentation was lacking.

To aid in the temperature estimates based on surface discoloration, five sets of calibration specimens were prepared as follows:

(a) Hastelloy X (0.008 in. Thick)

Temperatures: 1000°, 1100°, 1200°, 1300°, 1400°, 1500°, and 1600°F

Exposure time: 2 minutes

Surface preparation prior to exposure: none (as-received mill finish)

Cleaning prior to exposure: Freon

(b) Hastelloy X (0.008 in. Thick)

Temperatures: 1000°, 1100°, 1200°, 1300°, 1400°, 1500°, and 1600°F

Exposure time: 2 minutes

Surface preparation prior to exposure: Polished with "Crocus" cloth

Cleaning prior to exposure: Freon

(c) Hastelloy X (0.008 in. Thick)

Temperatures: 1000°, 1100°, 1200°, 1300°, 1400°, 1500°, and 1600°F

Exposure time: 10 minutes

Surface preparation prior to exposure: None (as-received mill finish); however, the area for the thermocouple attachment had been polished and thus, provided a calibration for this condition.

Cleaning prior to exposure: Freon

(d) Nickel Ni-200 (0.040 in. Thick)

Temperatures: 1000°, 1100°, 1200°, 1300°, 1400°, 1500°, and 1600°F

Exposure time: 2 minutes

Surface preparation prior to exposure: None (as-received mill finish)

Cleaning prior to exposure: Freon

(e) Nickel Ni-200 (0.040 in. Thick)

Temperatures: 1000°, 1100°, 1200°, 1300°, 1400°, 1500°, and 1600°F

Exposure time: 2 minutes

Surface preparation prior to exposure: Polished with "Crocus" cloth

Cleaning prior to exposure: Freon

(f) All Two-Minute Specimens

Specimens were placed in the furnace and an inert (nitrogen) atmosphere maintained until the desired exposure temperature was reached. At that point, oxygen, corresponding to that present in methane combustion products for equivalence ratio of 0.5, was introduced into the furnace with the nitrogen (90 percent nitrogen, 10 percent oxygen). Following the specified exposure time, oxygen flow was stopped and nitrogen flow maintained while the specimen cooled.

(g) Ten-Minute Specimens

Atmosphere was 90-percent nitrogen and 10-percent oxygen during heating and 10-minute exposure time. During cool-down time, a pure nitrogen atmosphere was used. The heating time was 10 minutes for all 10-minute exposures.

(h) All Specimens

Specimen temperatures were monitored by means of thermocouples welded to each of the specimens. Temperatures were recorded and monitored.

Figures 8.1-1 through 8.1-7 are diagrams of the discolorations observed on the SAM. The color descriptions are subjective and for reference only. The temperatures shown in the diagrams are the best estimates based on color comparisons at these temperatures and at bracketing temperatures. The calibration specimens used as the basis for the estimates are noted in the diagrams. Figure 8.1-6 also shows an area of localized yielding noted after Test 42, Run 26, but not present after Test 42, Run 19, when nozzle was removed for seal replacement.

8.1.2.2 Temperature-Indicating Paint

For two of the test runs, selected areas on the nozzle were polished with No. 400 grit paper, and temperature-indicating paint applied. Results are shown diagrammatically in Figures 8.1-6 and 8.1-7.

The low-temperature-range paint ("Thermindex" 0/E-94) was overheated and did not provide meaningful data, as shown in Figure 8.1-6. The high temperature paint ("Thermindex" 0/G-6) gave results which agreed reasonably well with observed metal discoloration for this run. On the subsequent run, however, the paint gave results which are not quantitatively valid, as shown in Figure 8.1-7. This may be due to a peculiarity of application or the effects of hydrogen injection during this run (no hydrogen was injected during the run for which results are shown in Figure 8.1-6). Distinct color patterns were obtained and may prove useful for qualitative analysis.

8.1.2.3 Leakage

The SAM hydrogen system was periodically checked for leakage using soap solution as the primary indication. Pressure decay tests became too insensitive following foreign object damage to the leading edge. The history of leak development is as follows, with all leak tests run at approximately 300 psia:

Post Test 41 - Run 28: Nozzle-inner shell port seals replaced because of excessive leakage. New seals showed no leakage.

Post Test 41 - Run 29: Minute leakage at trailing-edge end of Strut No. 5, between inner shell and strut.

Post Test 42 - Run 19: Nozzle-inner shell port seals showed excessive leakage. Replaced with rubber O-rings. New seals showed no leakage.

Post Test 42 - Run 25: Minute leakage at forward end of Strut No. 5, between outer shell and strut, approximately 0.5 in. aft of leading edge.

Post Test 42 - Run 30: Minute leakage at forward end of Strut No. 2, between inner shell and strut, approximately 0.5 in. aft of leading edge.

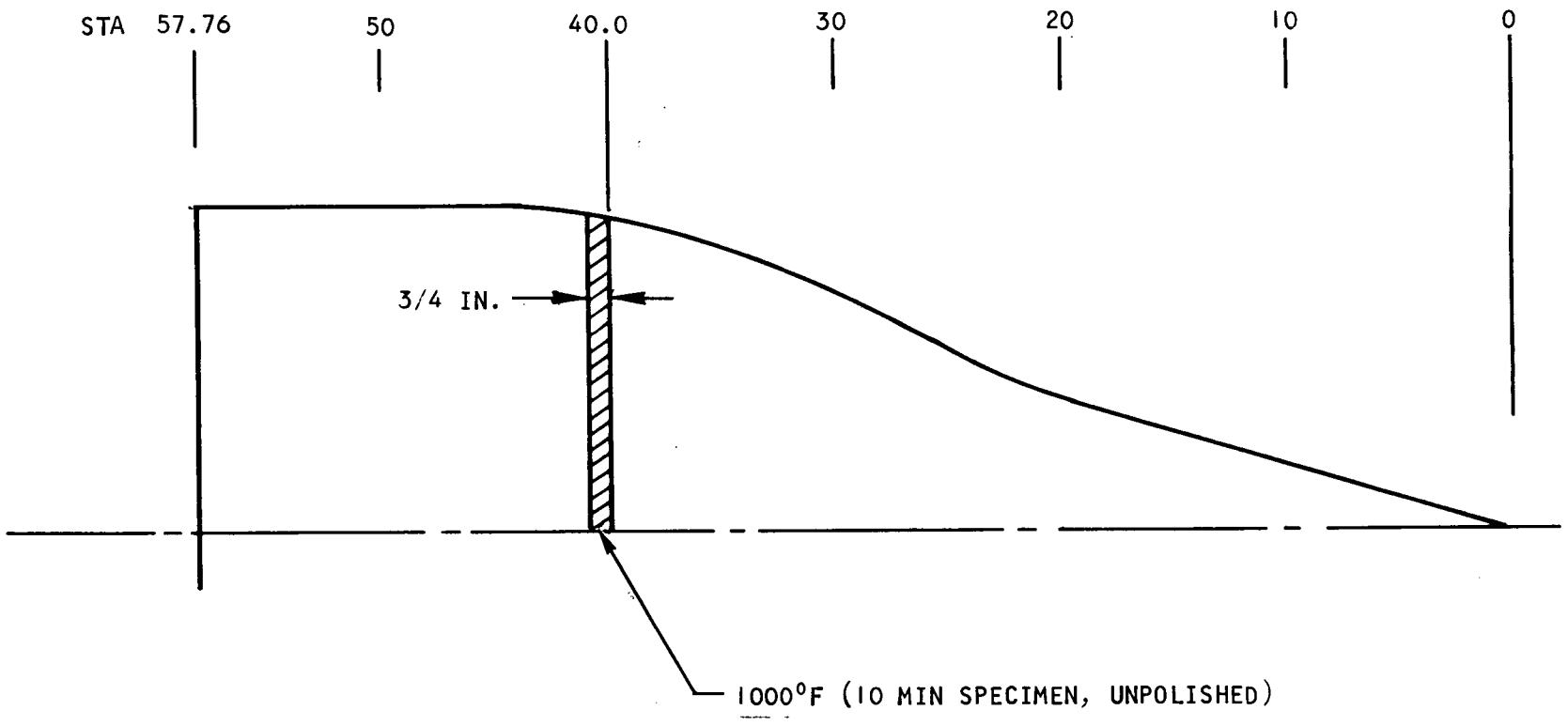

NOTES: 1. AREAS AFT OF STA 40 ARE NOT SUFFICIENTLY VISIBLE TO PERMIT INTERPRETATION OF COLORS
2. COMPARED POST TEST 42, RUN 36

S-63673

Figure 8.1-1. Spike Color Markings

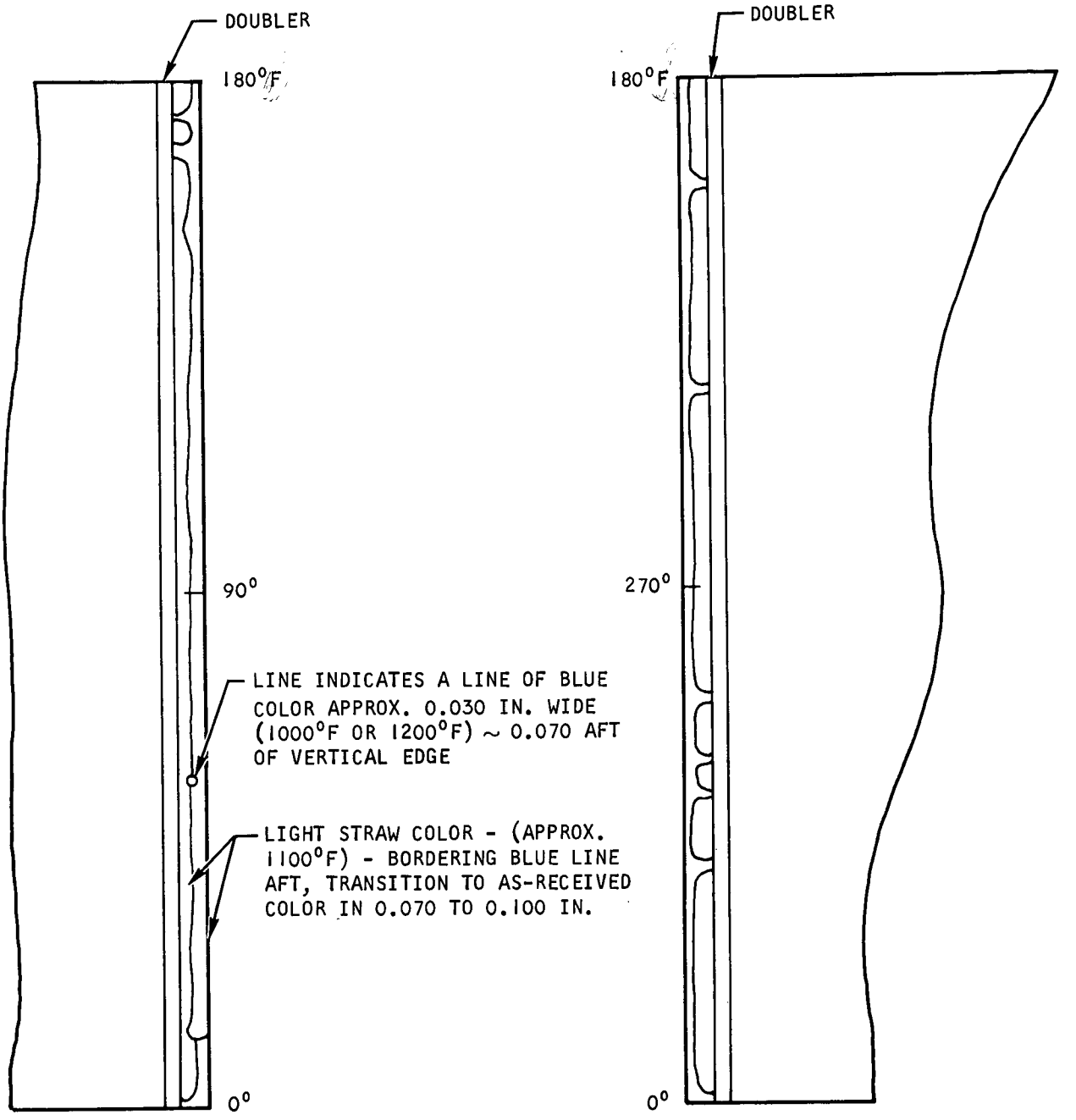

NOTES:
1. COMPARED POST TEST 42, RUN 36
2. ALL DISCOLORATION (BLUE) OCCURRED DURING TEST 41, RUN 26
3. INTERPRETATION BASED ON 2-MIN POLISHED AND UNPOLISHED NICKEL SPECIMENS

S-63675

Figure 8.1-2. Leading Edge External Surface Color Markings

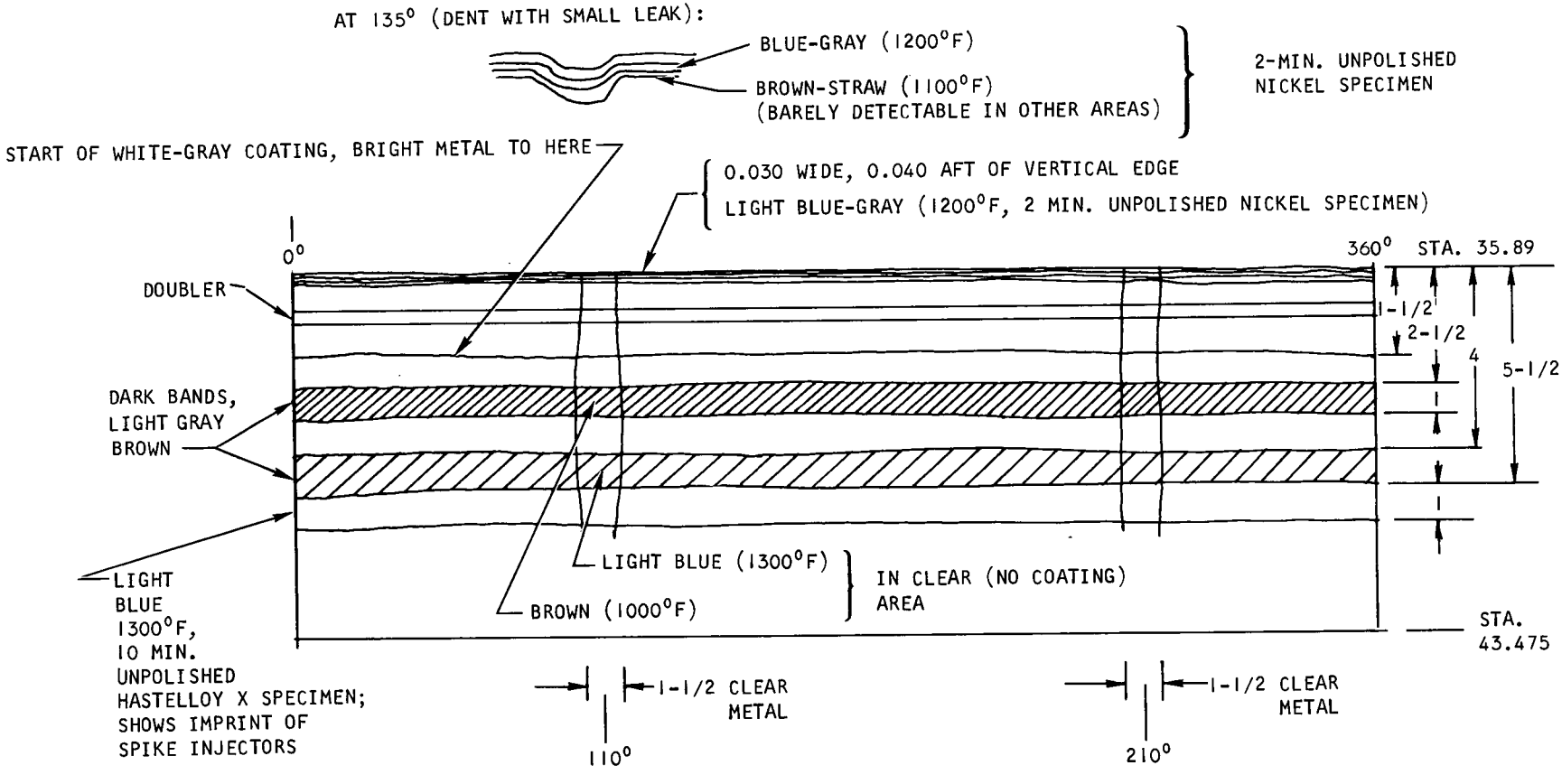

NOTES: 1. COMPARED POST TEST 42, RUN 36
2. ALL DIMENSIONS IN INCHES

S-63679

Figure 8.1-3. Leading Edge Internal Surface Color Markings

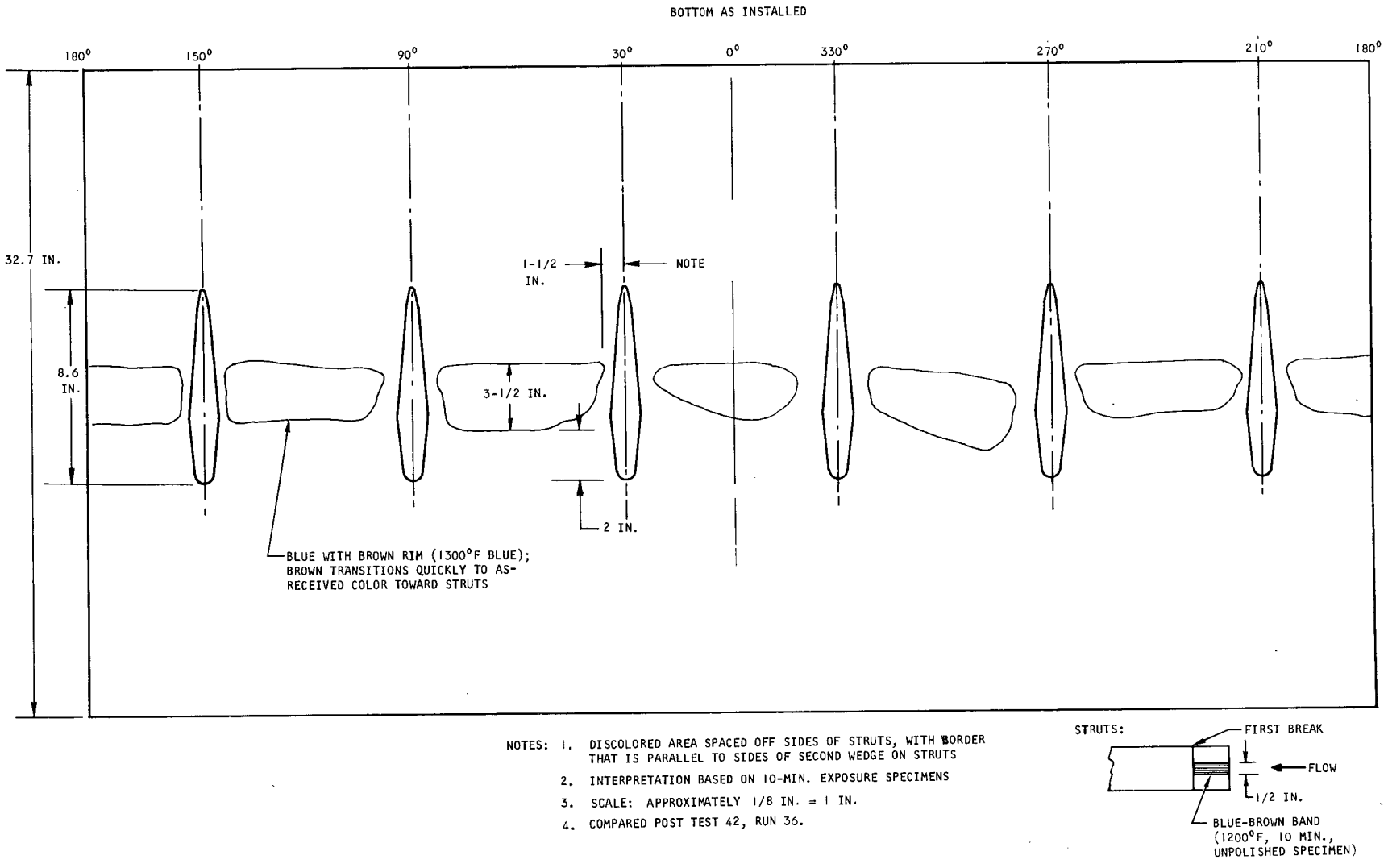

Figure 8.1-4. Outer Shell Color Markings

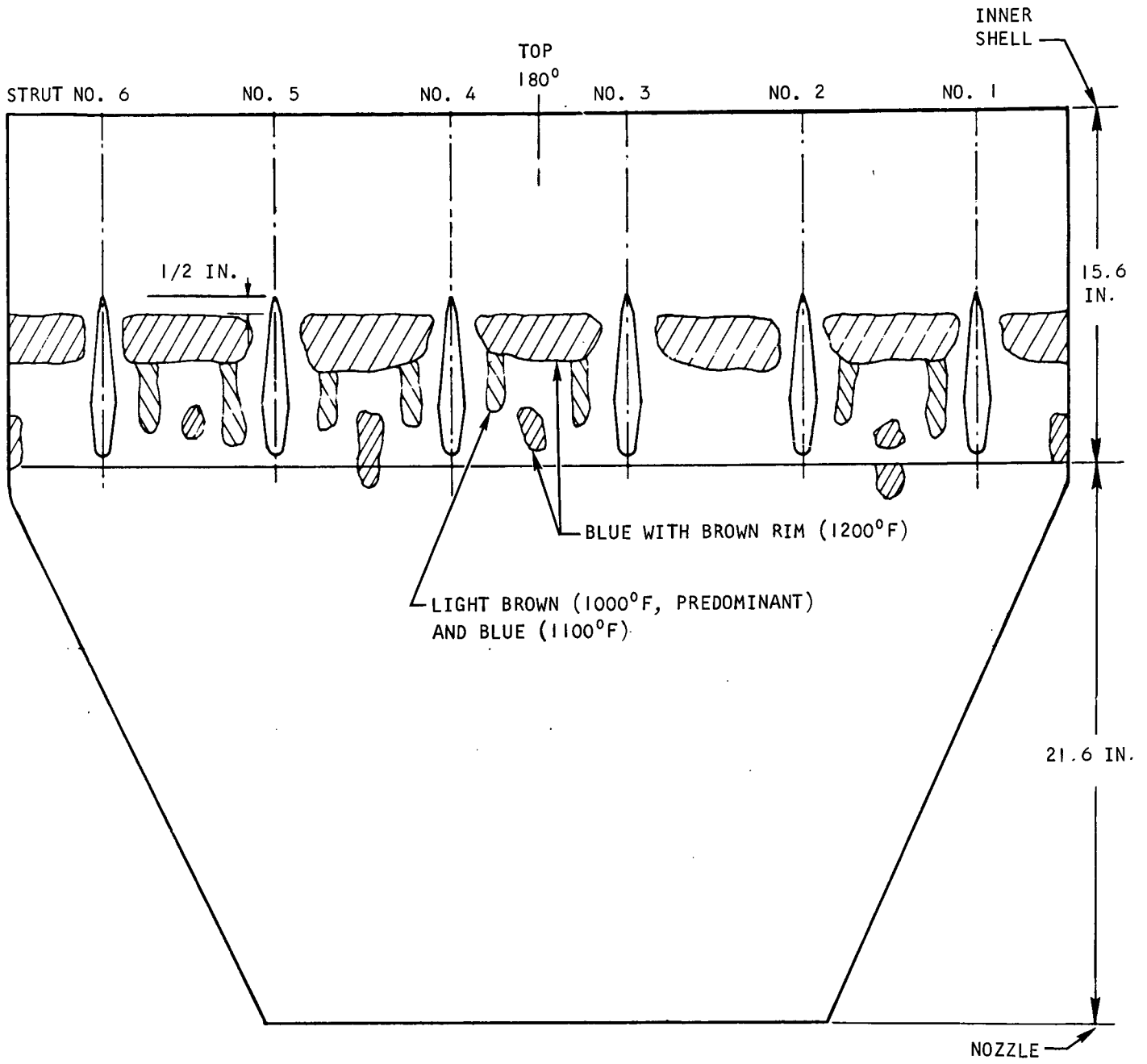

NOTES:
1. INTERPRETATION BASED ON 10-MIN UNPOLISHED SPECIMENS
2. SCALE: APPROXIMATELY 1/8 IN. = 1 IN.
3. COMPARED POST TEST 41, RUN 36

S-63677

Figure 8.1-5. Inner Body Color Markings

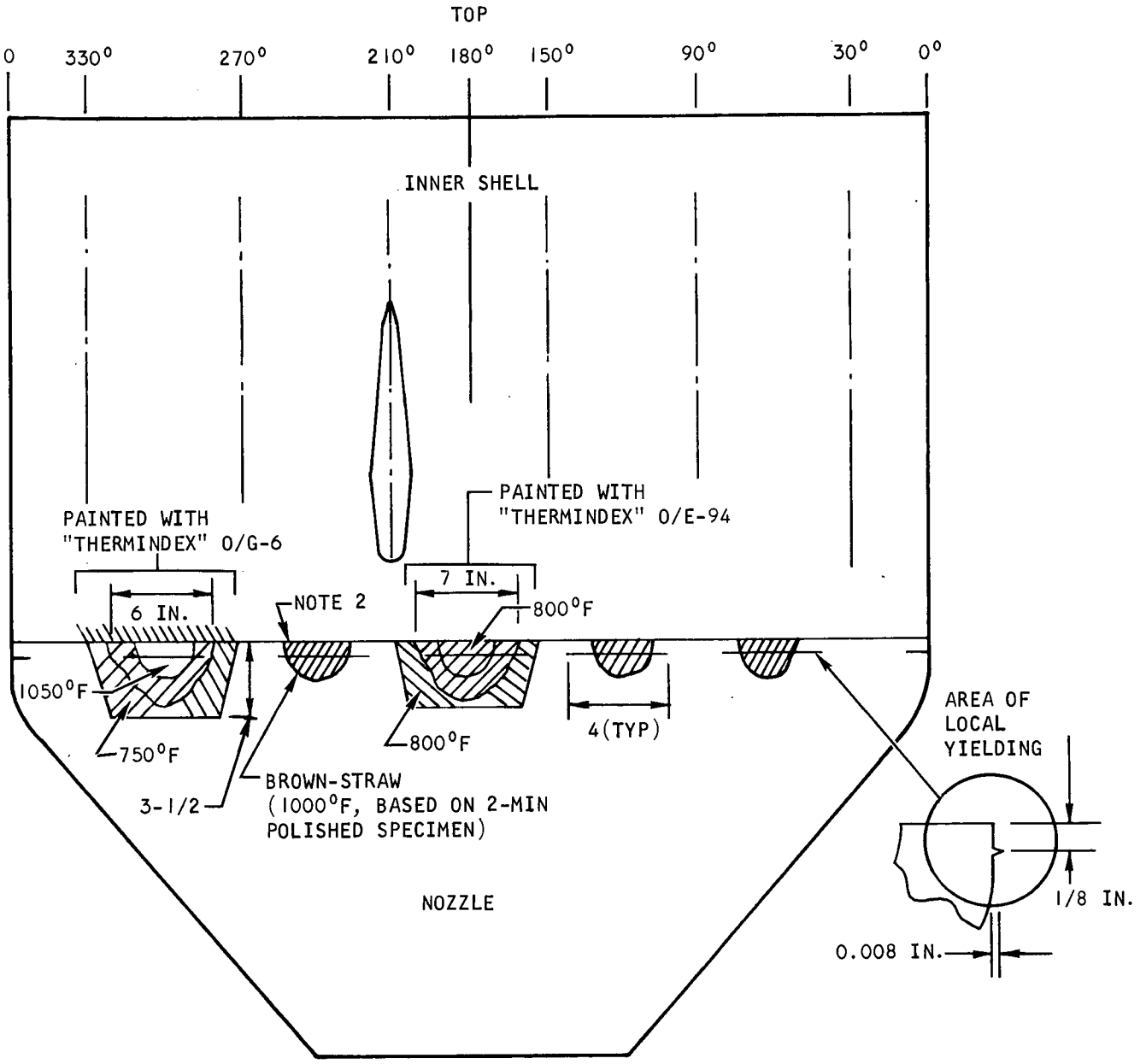

NOTES:
1. COMPARED POST TEST 42, RUN 34
2. THIS AREA POLISHED WITH "CROCUS" CLOTH TO REMOVE OXIDES PRIOR TO RUN 34

S-63674

Figure 8.1-6. Inner Body Discoloration

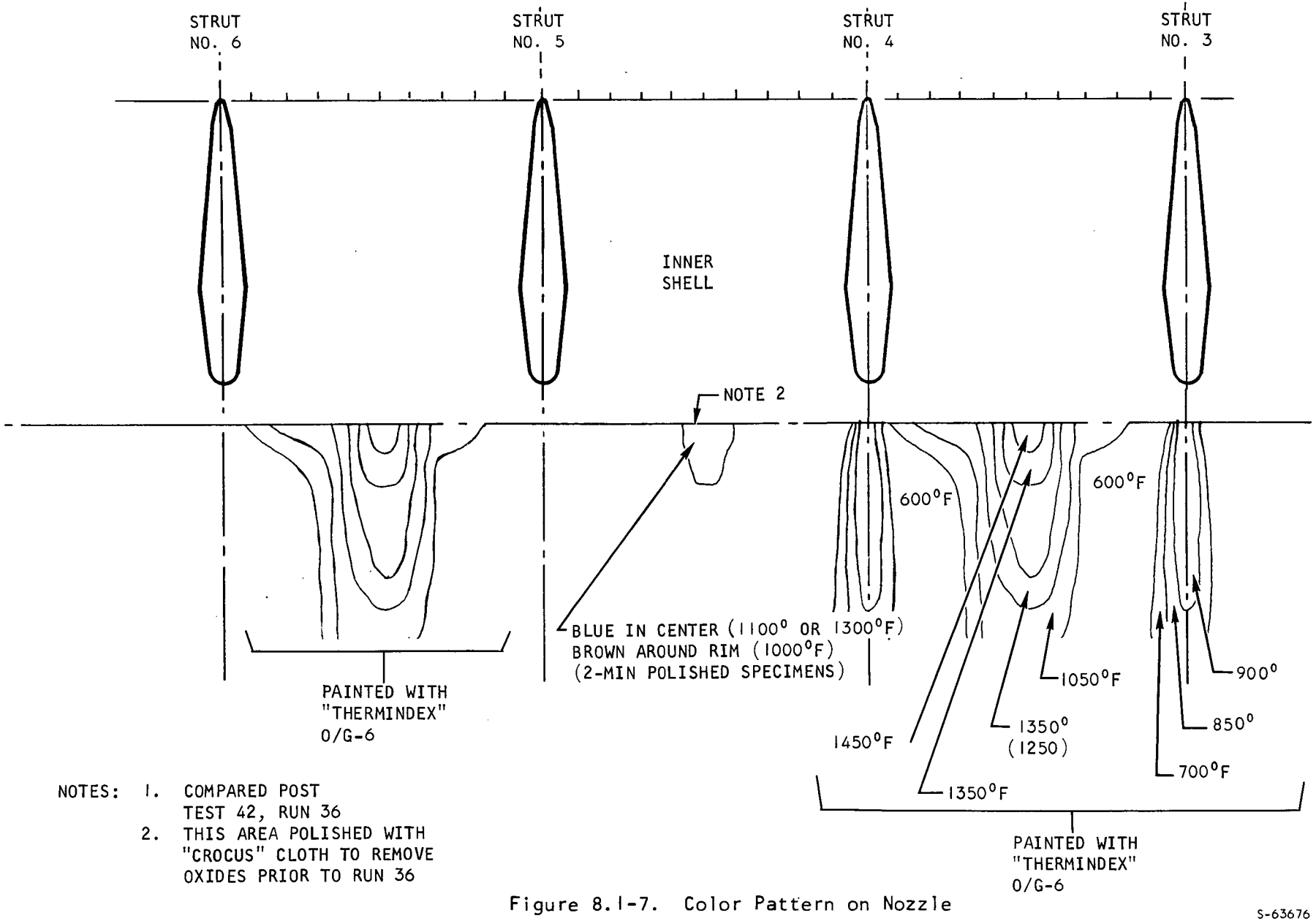

NOTES:
1. COMPARED POST TEST 42, RUN 36
2. THIS AREA POLISHED WITH "CROCUS" CLOTH TO REMOVE OXIDES PRIOR TO RUN 36

Figure 8.1-7. Color Pattern on Nozzle

Post Test 42 - Run 33: Leakage at forward end of Strut No. 3, between inner shell and strut, approximately 0.75 in. aft of leading edge. Leakage was sufficient to blow soap solution off area.

Post Test 42 - Run 36: Leakage at the aft end of the inner shell, at joint of inner shell and nozzle, midway between Struts No. 2 and 3. Leakage flow was blowing aft and may have been coming from joint of inner shell hot skin and coolant manifold.

Leading Edge: All leading edge leakage was caused by foreign object impingement and consisted of the following:

Test 41 - Run 20: Dent with hole; hole not visible to eye. Figure 7.1-2 shows this area.

Test 42 - Run 11: Clean penetration of skin, approximately 0.045 x 0.060 in. (Figure 7.1-1).

Test 41 - Run 27: Clean penetration of skin, approximately 0.010 in. diameter.

None of the leading edge leaks became worse in the course of testing. The areas of the leaks showed no signs of overheating relative to surrounding areas. In addition, none of the approximately 20 dents in the leading edge, all produced by foreign object impingement, showed signs of overheating. Figure 8.1-8 shows one of the larger dents.

8.1.2.4 Deformation

Detectable deformation of the hydrogen-cooled structure has occurred in three areas. These are:

(a) Local yielding in the nozzle hot skin, as shown in Figure 8.1-6.

(b) Distortion of the nozzle or inner shell, or both, at the interface of the two, as evidenced by interference during assembly and disassembly. This and Item (a) are related.

(c) Change in the gap between the leading edge and the spike, as shown in Figure 8.1-9.

8.2 HEAT TRANSFER PERFORMANCE

Heat transfer data reduction and analysis have been concentrated in the areas of (1) definition of the aerodynamic flow fields and correlation of aerodynamic heat transfer distributions from measured hot gas parameters, (2) comparison of hydrogen coolant heat loads with the correlated aerodynamic heat transfer rates, and (3) prediction of transient metal temperatures on the nozzle, aft outer shell and strut sides where locally high heating (metal discoloration) was observed.

F-13063

Figure 8.1-8. Dent in Leading Edge Produced by Foreign Object Impingement

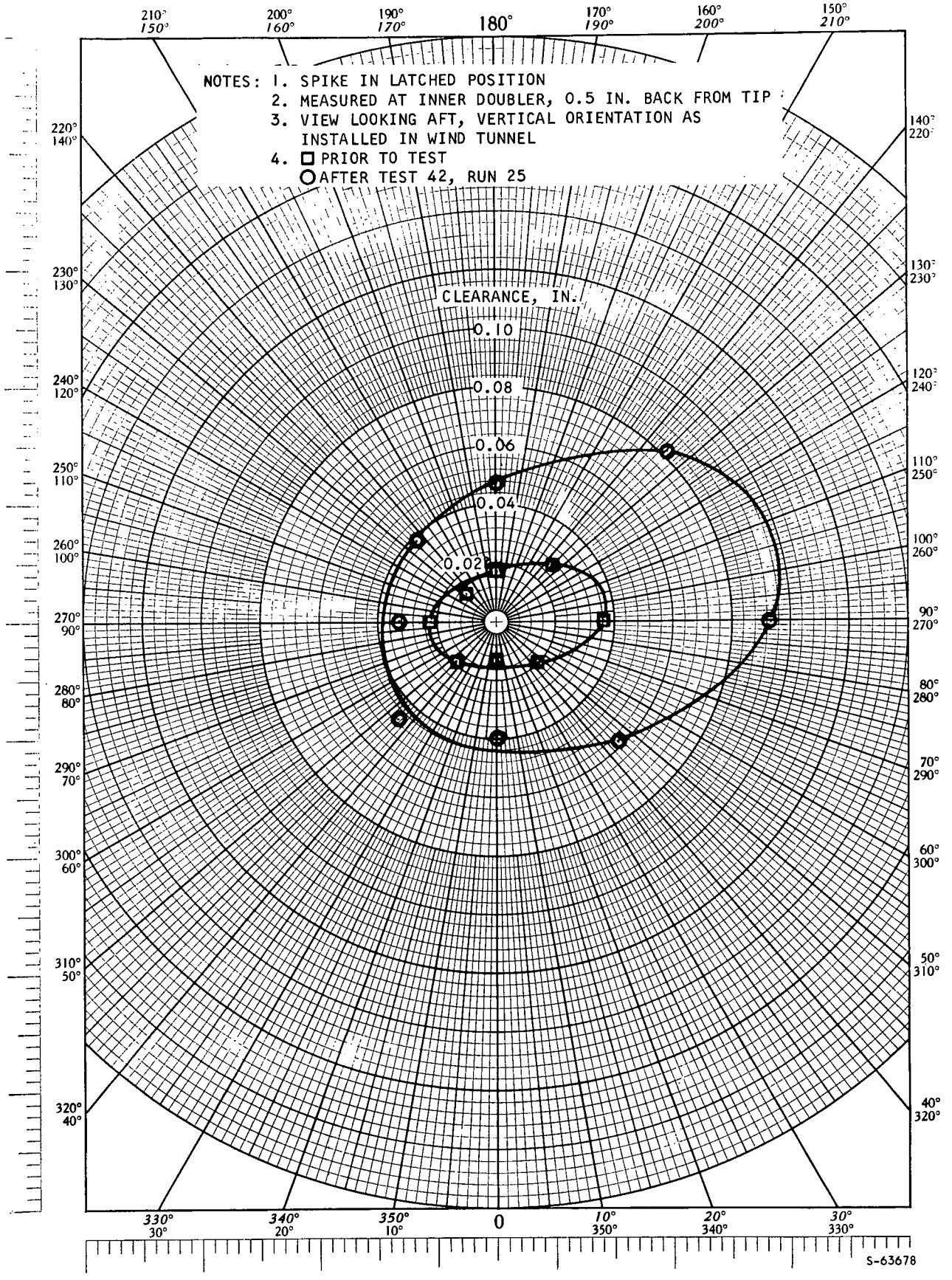

Figure 8.1-9. Clearance Between Leading Edge and Spike

8.2.1 Aerodynamic Heating

Preliminary analysis of the SAM aerodynamic heating has indicated fair agreement between the recommended theories and the experimental heat load on the spike, the inner shell, and the forward outer body. Comparison has not yet been made between the theories and the experimental results for the nozzle and the aft section of the outer shell, because structural temperatures in these areas have not reached steady-state for the tests performed to date. Shock interference patterns of larger-than-predicted-strength have occurred in the region of the strut. These shock patterns produced locally high heating areas on the forward part of the strut at the middle-third distance from the wall, on the outer shell between the struts, and on the nozzle-inner shell junction midway between two adjacent struts. Most other strong shock impingement areas have been previously predicted.

Some basic data have not been accurately determined at this time; vis, the freestream Mach number inlet mass-flow ratio, and the coolant flow rates in the innerbody and trailing edge routes at very low flowmeter frequencies. The data correlation presented herein, while qualitatively correct, will change quantitatively to reflect changes in estimates for the above parameters.

Experimental local heat fluxes are calculated from hot and cold wall thermocouple pairs that are located at 13 locations on the plate fin surfaces of the model. The calculation procedure is discussed in Section 8.2.3.1. Average heat fluxes are calculated from hydrogen coolant thermocouples located at the inlet and outlet of each flow route. At intermediate locations along the flow routes, cold wall thermocouples are used instead of coolant thermocouples to calculate average heat flux. During thermal transients (such as on the inner shell) average hot gas heat load is estimated by including the heat capacity of the structure in the calculation.

The hot gas pressure distribution between the center and outer bodies is not linear between pressure tap locations because of shock interference patterns. Although the local pressure is known, the local velocity cannot be accurately determined because (1) there is no total-pressure measurement, (2) the inlet mass flow ratio is not accurately known, and (3) the flow is not uniform across the duct. The one-dimensional flow solution is not accurate for localized flow calculations. The existence of shock waves in the inlet can be seen from the Schlieren photograph, Figure 8.2-1, which shows an oblique shock inclining approximately at 24 deg relative to the engine centerline. In addition, a moderately strong shock emanates from the cowl tip due to the finite bluntness of the tip. The evidence of the strong shocks persisting into the duct at Station X = 44 is seen in Figure 8.2-2 in which the local outer shell and inner shell pressure and the spike position are plotted vs time for Test 41, Run 7, 65 sec. When the spike is 2.2 inches from the fully extended position, the outer wall pressure (P25) reads 3.4 psia, while the inner wall pressure (P86) reads 5.7 psia. The two pressure levels interchange when the spike is retracted an additional half-inch. This interchange indicates that there is a strong shock near the engine throat (X = 44). Based on the shock emanating from spike compression surface (Figure 8.2-1), the inlet zone flow field was constructed by the method of characteristics. The angle of the internal shock originating at the cowl

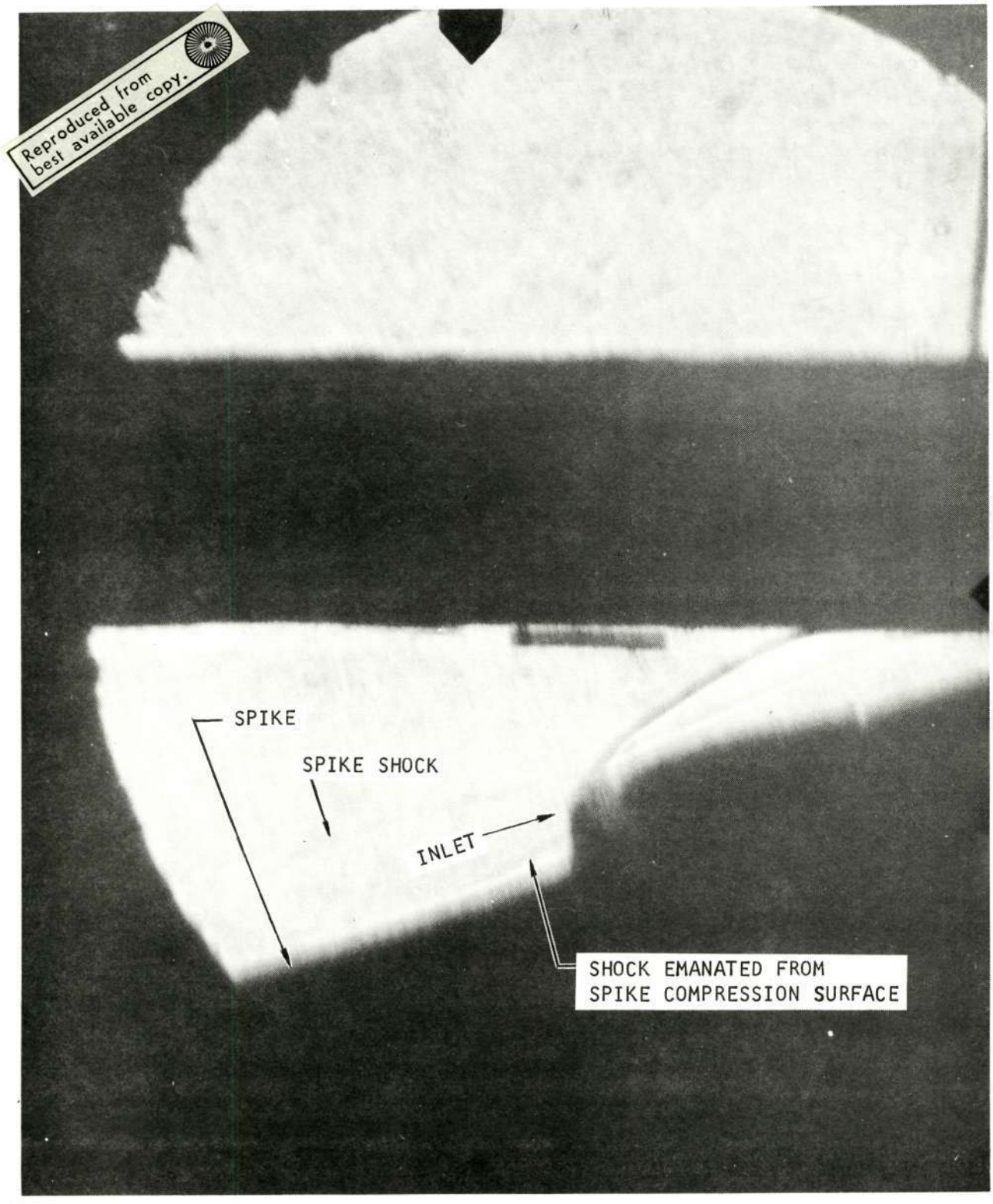

Figure 8.2-1. Typical Schlieren Photograph of Cowl Leading Edge Region

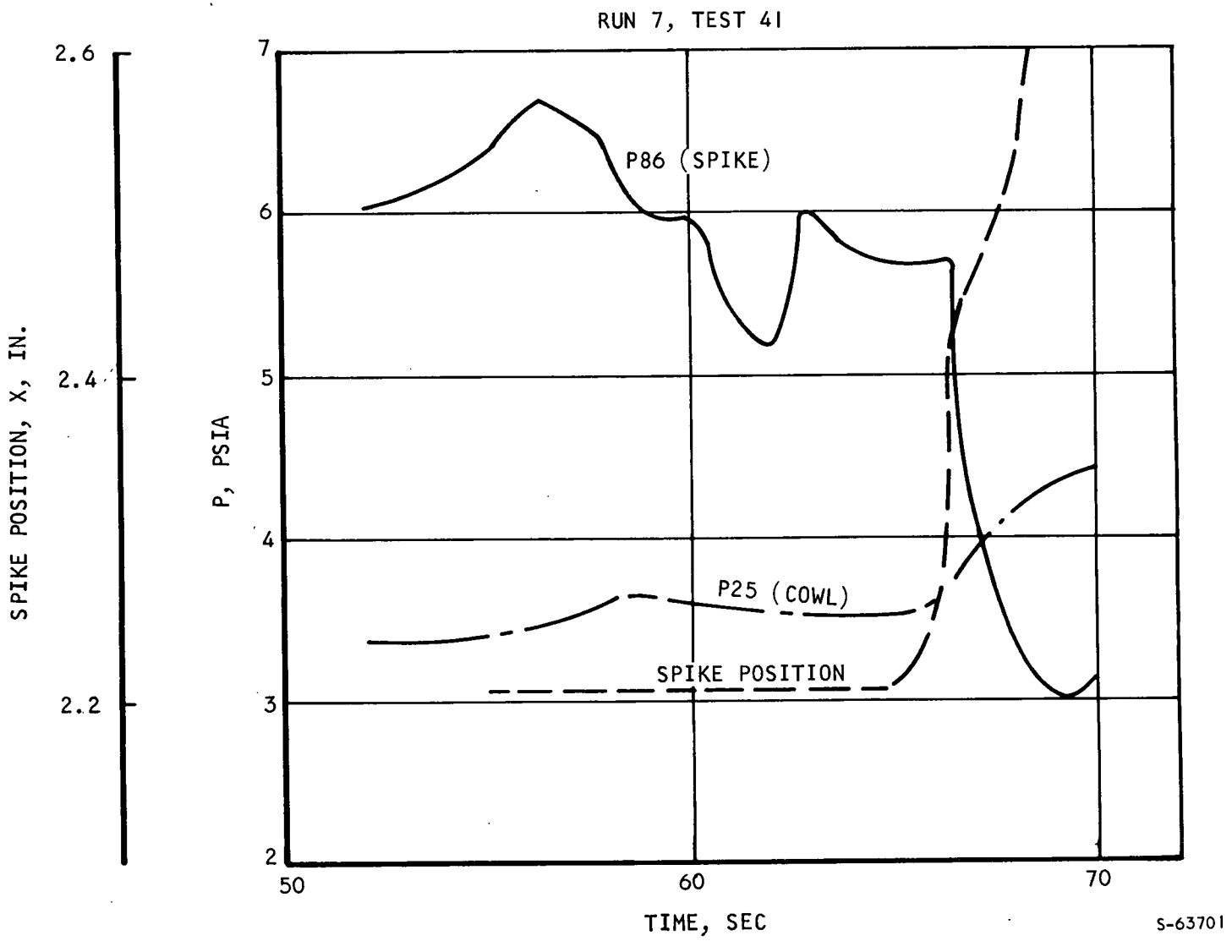

Figure 8.2-2. Pressure at Station 44 vs Spike Position

leading edge was determined as 17-1/2 deg relative to the approaching flow. Shown in Figure 8.2-3 is the estimated flow field for Test 41, Run 20, based, for this preliminary evaluation, on one-dimensional duct velocity calculations.

The experimental and theoretical heat loads for Test 41, Runs 4, 13, 17, and 20, are shown in Tables 8.2-1 and 8.2-2 for the spike, inner shell, and leading edge/forward outer shell. Also, heat loads rather than local heat flux are used for correlation because large heat flux gradients prevail in the areas of shock impingement. The exact locations of thermocouples relative to the shock impinging point are uncertain. The resulting theoretical-to-experimental heat loads are shown in Figure 8.2-4. The methods of aerodynamic heat transfer calculation are discussed below.

For the spike straight section, the laminar flow heat transfer is $\sqrt{3}$-times the Eckert flat-plate value. For turbulent flow, the heat transfer is 2-1/5-times the flat-plate value. For the flat plate turbulent flow, the reference enthalpy technique is used to account for the compressibility factor; i.e., the thermodynamic and the transport properties are evaluated at a temperature corresponding to the reference enthalpy. Two methods are used to evaluate the reference enthalpy; (1) Eckert's reference method and (2) adiabatic reference method.

Eckert's reference enthalpy is

$$H_{aw} = H_\infty + Pr^{1/3} (H_T - H_\infty) \qquad (8\text{-}1)$$

$$H^* = H_\infty + 1/2 (H_W - H_\infty) + 0.22 (H_r - H_\infty) \qquad (8\text{-}2)$$

The adiabatic value is obtained by replacing the wall enthalpy (H_W) in Equation (8-2) with the adiabatic wall enthalpy (H_{aw}) to get

$$H^* = 0.28 H_\infty + 0.72 (H_r - H_\infty) \qquad (8\text{-}3)$$

Subscripts, ∞, T, aw, W and * refer to freestream static, freestream stagnation, adiabatic wall, wall and reference conditions, respectively. Pr is Prandtl number.

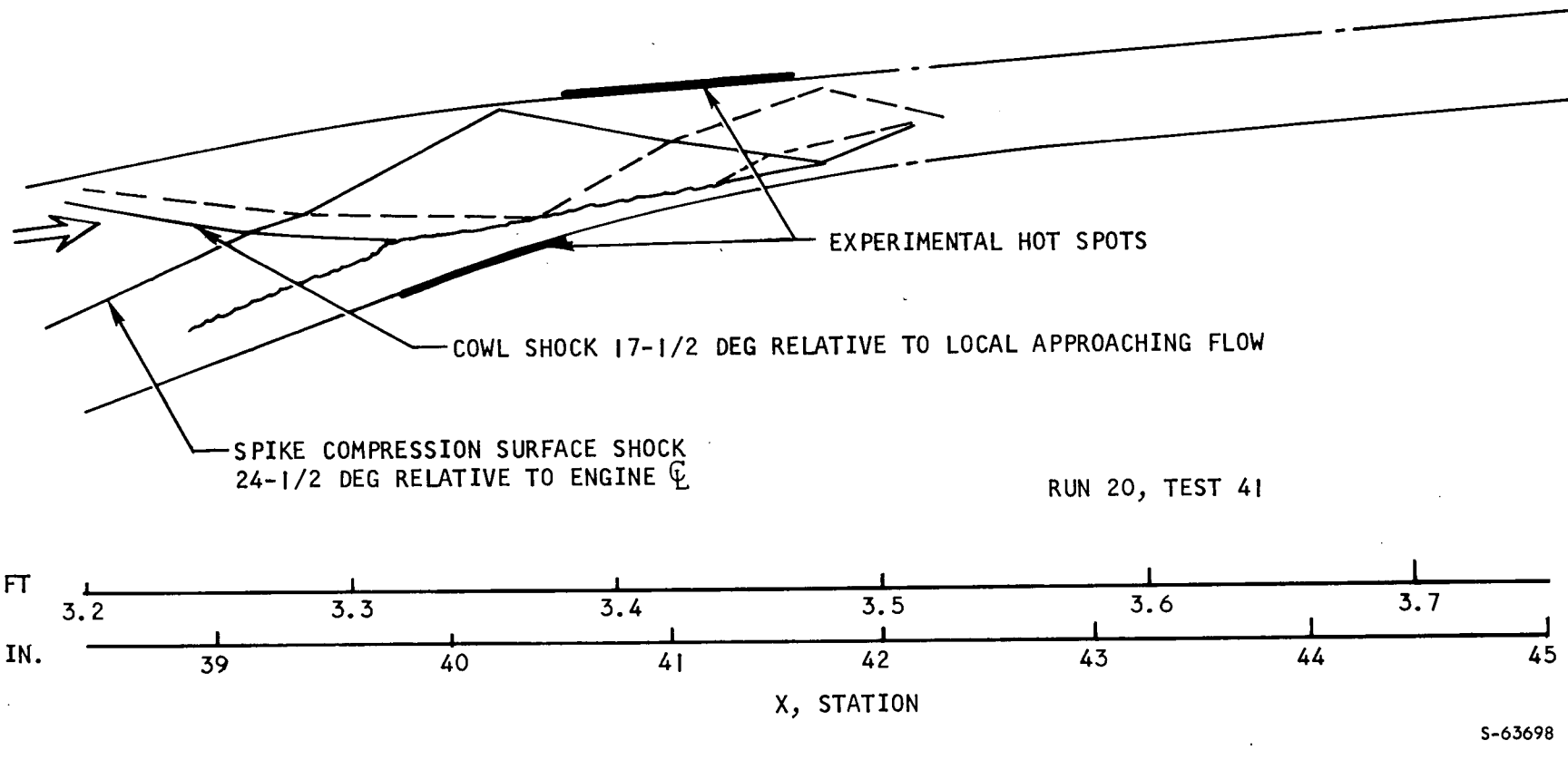

Figure 8.2-3. Approximate Flow Field at the Inlet Station

TABLE 8.2-1

CENTERBODY HEAT TRANSFER

Test 41 Run 7 Data acquisition time = 62.0 sec
Tunnel total pressure = 961 psia Tunnel total temperature = 2689°R
Spike translation from latched position = 2.20 in.
Axial location of laminar/turbulent boundary layer transition = 18.9 in.
Axial location of turbulent boundary layer virtual origin = 15.9 in.

	Component	Spike				Inner Shell
	H_2 flow rate, lb/sec	0.116				0.0234
	Axial locations X_1 to X_2, (ref. coord.), in.	0.60 to 35.7	35.7 to 40.5	40.5 to 44.3	43.0 to 55.8	55.8 to 65.6
	H_2 temp. at X_2, °R	623	715	904	1196	919
	H_2 temp, at X_1, °R	532	629	715	904	646
①	H_2 heat load from X_1 to X_2, Btu/sec	39.5	35.0	76.7	119.0	22.0
	Avg. structural temp. rise from X_1 to X_2, °R/sec	-	-	-	-	6.5
②	Structural heat sink rate from X_1 to X_2, Btu/sec	-	-	-	-	16.2
	Test heat load, Btu/sec (sum of ① and ②)	39.5	35.0	76.7	119.0	38.2
③	Avg. test heat flux from X_1 to X_2, Btu/sec ft^2	7.9	20.6	48.0	23.8	8.1
④	Calculated avg. heat flux (adiabatic wall ref. enthalpy) from X_1 to X_2, Btu/sec ft^2	6.2	22.4	35.3	26.2	7.5
	Calculated avg. heat flux (Eckert's ref. enthalpy) from X_1 to X_2, Btu/sec ft^2	8.7	31.8	48.0	35.2	10.4
⑤	Local test heat flux at X_2, Btu/sec ft^2	12.3				
⑥	Calculated local flux (adiabatic wall ref. enthalpy) at X_2, Btu/sec ft^2	12.3	-	-	-	-
	Local calculated-to-test heat flux ratio (⑥ / ⑤)	1.0	-	-	-	-
	Avg. calculated-to-test heat flux ratio (④ / ③)	0.78	1.09	0.74	1.10	0.92

TABLE 8.2-1 (Continued)

Test 41 Run 13 Data acquisition time = 68.0 sec
Tunnel total pressure = 910 psia Tunnel total temperature = 2637°R
Spike translation from latched position = 2.89 in.
Axial location of laminar/turbulent boundary layer transition = 15.4 in.
Axial location of turbulent boundary layer virtual origin = 13.0 in.

	Component	Spike				Inner Shell
	H_2 flow rate, lb/sec	0.133				0.0111
	Axial locations X_1 to X_2, (ref. coord.), in.	0.60 to 35.7	35.7 to 40.5	40.5 to 44.3	44.3 to 55.8	55.8 to 65.6
	H_2 temp. at X_2, °R	590	653	791	1039	872
	H_2 temp. at X_1, °R	508	590	653	791	621
①	H_2 heat load from X_1 to X_2, Btu/sec	38.0	29.2	64.0	115.0	9.8
	Avg. structural temp. rise from X_1 to X_2, °R/sec	-	-	-	-	8.4
②	Structural heat sink rate from X_1 to X_2, Btu/sec	-	-	-	-	20.9
	Test heat load, Btu/sec (sum of ① and ②)	38.0	29.2	64.0	115.0	30.7
③	Avg. test heat flux from X_1 to X_2, Btu/sec ft^2	7.6	17.2	40.0	23.0	6.5
④	Calculated avg. heat flux (adiabatic wall ref. enthalpy) from X_1 to X_2, Btu/sec ft^2	6.4	22.0	34.8	27.4	7.3
	Calculated avg. heat flux (Eckert's ref. Enthalpy) from X_1 to X_2, Btu/sec ft^2	9.1	32.2	49.5	38.0	10.4
⑤	Local test heat flux at X_2, Btu/sec ft^2	14.0	-	-	-	-
⑥	Calculated local flux (adiabatic wall ref. Enthalpy) at X_2, Btu/sec ft^2	12.3	-	-	-	-
	Local calculated-to-test heat flux ratio (⑥ / ⑤)	0.88	-	-	-	-
	Avg. calculated-to-test heat flux ratio (④ / ③)	0.84	1.28	0.87	1.20	1.12

TABLE 8.2-1 (Continued)

Test 41 Run 17 Data acquisition time = 76.0 sec
Tunnel total pressure = 1287 psia Tunnel total temperature = 2850°R
Spike translation from latched position = 2.88 in.
Axial location of laminar/turbulent boundary layer transition = 19.5 in.
Axial location of turbulent boundary layer virtual origin = 15.5 in.

	Component	Spike				Inner Shell
	H_2 flow rate, lb/sec	0.193				0.0132
	Axial locations X_1 to X_2, (ref. coord.), in.	0.60 to 35.7	35.7 to 40.5	40.5 to 44.3	44.3 to 55.8	55.8 to 65.6
	H_2 temp. at X_2, °R	612	676	823	1083	1152
	H_2 temp. at X_1, °R	526	612	676	823	741
①	H_2 heat load from X_1 to X_2, Btu/sec	58.0	43.3	100.0	176.0	19.0
	Avg. structural temp. rise from X_1 to X_2, °R/sec	-	-	-	-	9.0
②	Structural heat sink rate from X_1 to X_2, Btu/sec	-	-	-	-	22.0
	Test heat load, Btu/sec (sum of ① and ②)	58.0	43.3	100.0	176.0	41.0
③	Avg. test heat flux from X_1 to X_2, Btu/sec ft^2	11.6	22.5	62.5	35.2	8.7
④	Calculated avg. heat flux (adiabatic wall ref. enthalpy) from X_1 to X_2, Btu/sec ft^2	10.3	34.3	61.5	40.2	10.4
	Calculated avg. heat flux (Eckert's ref. enthalpy) from X_1 to X_2, Btu/sec ft^2	15.1	50.7	88.5	55.7	14.7
⑤	Local test heat flux at X_2, Btu/sec ft^2	18.4	-	-	-	-
⑥	Calculated local flux (adiabatic wall ref. enthalpy) at X_2, Btu/sec ft^2	19.1	-	-	-	-
	Local calculated-to-test heat flux ratio (⑥ / ⑤)	1.04	-	-	-	-
	Avg. calculated-to-test heat flux ratio (④ / ③)	0.89	1.34	0.99	1.14	1.20

TABLE 8.2-1 (Continued)

Test 41 Run 20 Data acquisition time = 76.0 sec
Tunnel total pressure = 1534 psia Tunnel total temperature = 2768°R
Spike translation from latched position = 2.86 in.
Axial location of laminar/turbulent boundary layer transition = 15.5 in.
Axial location of turbulent boundary layer virtual origin = 13.1 in.

	Component	Spike				Inner Shell
	H_2 flow rate, lb/sec	0.184				0.0144
	Axial locations X_1 to X_2, (ref. coord.), in.	0.60 to 35.7	35.7 to 40.5	40.5 to 44.3	44.3 to 55.8	55.8 to 65.6
	H_2 temp. at X_2, °R	618	694	859	1157	1139
	H_2 temp. at X_1, °R	515	618	694	859	729
①	H_2 heat load from X_1 to X_2, Btu/sec	66.3	49.0	106.0	192.0	20.6
	Avg. structural temp. rise from X_1 to X_2, °R/sec	-	-	-	-	8.6
②	Structural heat sink rate from X_1 to X_2, Btu/sec	-	-	-	-	21.5
	Test heat load, Btu/sec (sum of ① and ②)	66.3	49.0	106.0	192.0	42.1
③	Avg. test heat flux from X_1 to X_2, Btu/sec ft^2	13.3	28.8	66.0	38.4	9.0
④	Calculated avg. heat flux (adiabatic wall ref. enthalpy) from X_1 to X_2, Btu/sec ft^2	11.5	29.4	52.2	43.0	11.0
	Calculated avg. heat flux (Eckert's ref. enthalpy) from X_1 to X_2, Btu/sec ft^2	15.4	44.0	74.0	58.8	15.3
⑤	Local test heat flux at X_2, Btu/sec ft^2	20.5	-	-	-	-
⑥	Calculated local flux (adiabatic wall ref. enthalpy) at X_2, Btu/sec ft^2	19.1	-	-	-	-
	Local calculated-to-test heat flux ratio (⑥ / ⑤)	0.93	-	-	-	-
	Avg. calculated-to-test heat flux ratio (④ / ③)	0.87	1.02	0.79	1.12	1.22

TABLE 8.2-2

FORWARD OUTERBODY* HEAT TRANSFER

Test 41 Run 7 Data acquisition time = 62.0 sec

Tunnel total pressure = 961 psia Tunnel total temperature = 2689°R

Spike translation from latched position = 2.20 in.

H_2 Flow rate, lb/sec	0.0398	
Axial locations X_1 to X_2 (ref. coord.), in.	35.9 to 46.0	46.0 to 50.4
Axial distances from cowl L.E., in.	0.0 to 11.1	11.1 to 14.5
H_2 temp. at X_2, °R	1189	1613
H_2 temp. at X_1, °R	743	1189
① H_2 heat load from X_1 to X_2, Btu/sec	62.2	59.0
② Calculated heat load (adiabatic wall reference enthalpy) from X_1 to X_2, Btu/sec	64.4	57.8
③ Local test heat flux at X_2, Btu/sec ft^2	24.8	50.8
④ Calculated local heat flux (adiabatic wall reference enthalpy) at X_2, Btu/sec ft^2	19.8	15.7
Local calculated-to-test heat flux ratio (④ / ③)	0.80	0.31
Calculated-to-test heat load ratio (② / ①)	1.04	0.98

*Internal surface of leading edge and forward outer shell.

TABLE 8.2-2 (Continued)

Test 41 Run 13 Data acquisition time = 68.0 sec

Tunnel total pressure = 910 psia Tunnel total temperature = 2637°R

Spike translation from latched position = 2.89 in.

H_2 Flow rate, lb/sec	0.0773	
Axial locations X_1 to X_2 (ref. coord.), in.	35.9 to 46.0	46.0 to 50.4
Axial distances from cowl L.E., in.	0.0 to 11.1	11.1 to 14.5
H_2 temp. at X_2, °R	1026	1299
H_2 temp. at X_1, °R	642	1026
① H_2 heat load from X_1 to X_2, Btu/sec	104.0	74.0
② Calculated heat load (adiabatic wall reference enthalpy) from X_1 to X_2, Btu/sec	95.0	75.1
③ Local test heat flux at X_2, Btu/sec ft^2	27.8	15.1
④ Calculated local heat flux (adiabatic wall reference enthalpy) at X_2, Btu/sec ft^2	26.4	16.5
Local calculated-to-test heat flux ratio (④ / ③)	0.95	1.10
Calculated-to-test heat load ratio (② / ①)	0.91	1.01

TABLE 8.2-2 (Continued)

Test 41 Run 17 Data acquisition time = 76.0 sec

Tunnel total pressure = 1287 psia Tunnel total temperature = 2850°R

Spike translation from latched position = 2.89 in.

	H_2 Flow rate, lb/sec	0.119	
	Axial locations X_1 to X_2 (ref. coord.), in.	35.9 to 46.0	46.0 to 50.4
	Axial distances from cowl L.E., in.	0.0 to 11.1	11.1 to 14.5
	H_2 temp. at X_2, °R	1062	1316
	H_2 temp. at X_1, °R	623	1062
①	H_2 heat load from X_1 to X_2, Btu/sec	183.0	106.0
②	Calculated heat load (adiabatic wall reference enthalpy) from X_1 to X_2, Btu/sec	169.5	120.0
③	Local test heat flux at X_2, Btu/sec ft^2	34.3	28.4
④	Calculated local heat flux (adiabatic wall reference enthalpy) at X_2, Btu/sec ft^2	41.0	27.5
	Local calculated-to-test heat flux ratio (④ / ③)	1.20	0.97
	Calculated-to-test heat load ratio (② / ①)	0.93	1.13

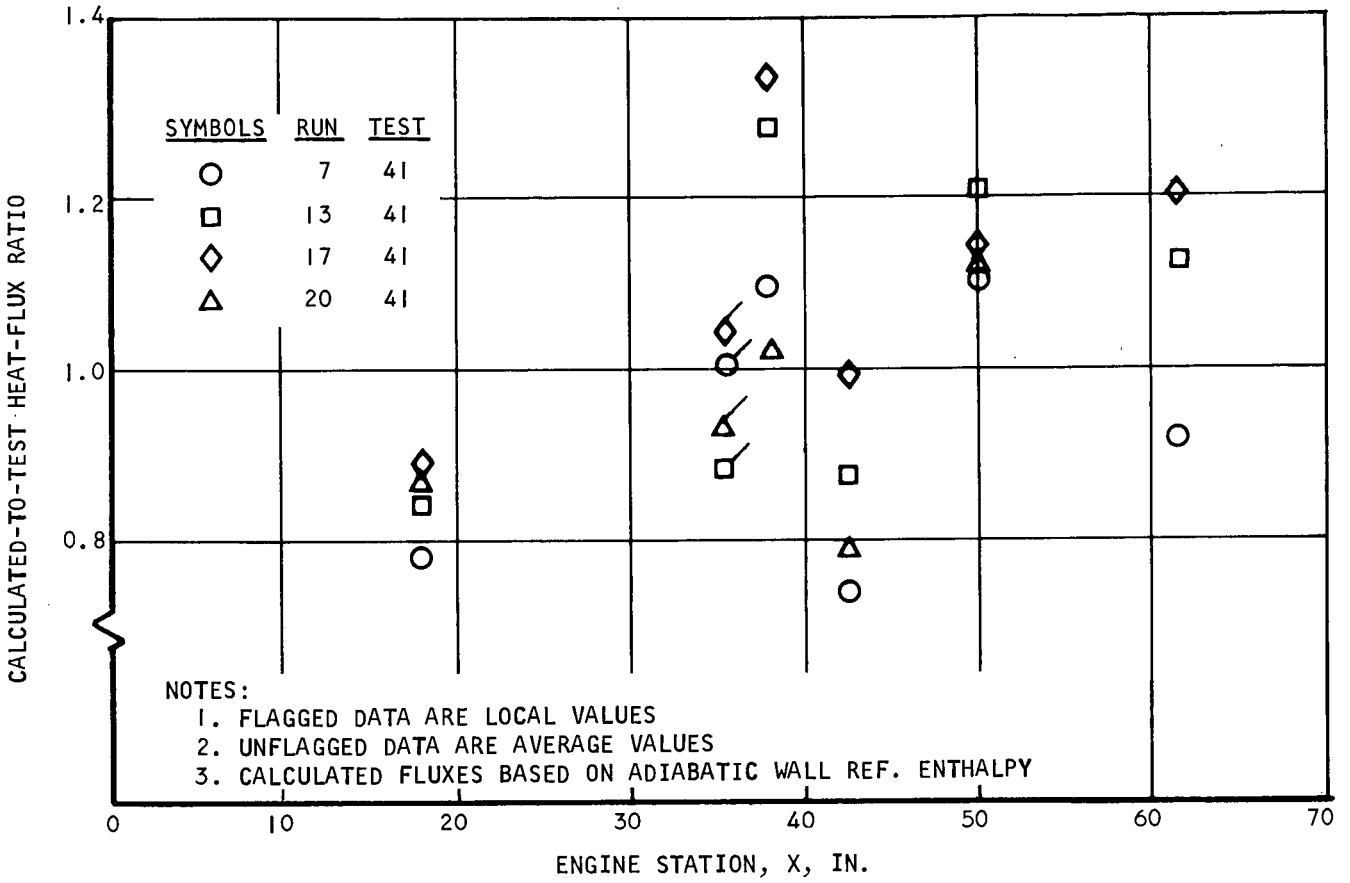

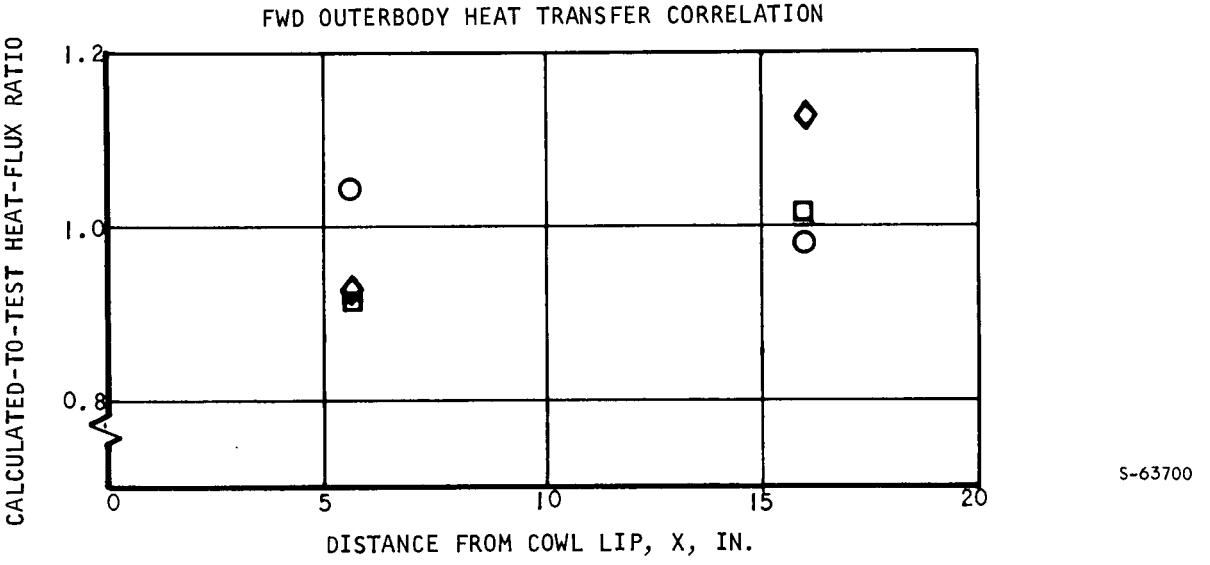

Figure 8.2-4. Spike and Inner Shell Heat Transfer Correlations

C.2

For the spike straight section the experimental heat loads and heat fluxes are obtained from the hot wall and cold wall thermocouple pairs at Station X = 35. Since the laminar boundary layer and the turbulent boundary layer heat transfer over a cone are relatively predictable, the experimental data permit the determination of the transition-Reynolds number. It is found the transition-Reynolds number is approximately 3,000,000 and that the transition is at approximately X = 20. The virtual origin of the turbulent boundary layer, which is obtained by equating the laminar and turbulent boundary layer momentum thicknesses at transition, is approximately 2 inches upstream of the transition point and is used in the cone solution. The cone solution is extended to Station X = 38 even though there is a pressure gradient. Between Stations 38 and 40, the turbulent flat-plate equation is used. From Stations X = 40 to 66, the turbulent duct equation is used. Heat transfer analyses aft of Station X = 66 have not been carried out, as yet, because the shock interference patterns and transient structural effects, discussed above, have added to complexities of a direct comparison. For the test data reduced to date, the adiabatic reference-enthalpy method, Equation (8-3), yields considerably better agreement than Eckert's method, Equation (8-2).

The areas of high heating in the vicinity of the struts are shown in Figure 8.2-5 which is sketched from observing the areas of discoloration after Test 42, Run 36. The high heating in these areas is caused by either shock impingement or by flow interference. There are six struts and an aft-facing step (at the end of the spike) that produce shock waves. Some surfaces will have more than one shock sweeping by. An approximate solution for the flow field by the method of characteristics was carried out in these regions, as shown in Figure 8.2-6. The estimated Mach number at Station X = 50 is 3.3. Rarefaction waves emanate from the inner body at X = 50, and from the end of the spike. The compression waves emanate from the inner body immediately downstream of the reattachment point of the separated base flow. These solutions are for a two-dimensional channel without the strut and without fuel injection. Since burning will reduce the flow Mach number, somewhat different shock patterns for Test 42 than shown in Figure 8.2-6 are expected.

The shock wave due to the presence of the strut alone (without other shocks) is shown in Figure 8.2-7 for two different local Mach numbers. There are areas in the vicinities of the strut that will have both the base recompression shock and the strut shock waves sweeping by. When this occurs, higher heating will result. Two such locations are marked in Figure 8.2-5. Areas marked A_i and B_o received the recompression shock from the base flow only. Area A_o, in addition to receiving the recompression shock, also received the wedge shock off the strut. Areas marked B_i appear to have been the intersection points of the shocks from two adjacent struts, and of the recompression base shock which is being reflected from the outer shell. Areas N_i and N_o are unaffected by shock impingement. Preliminary estimate of the increased heating in these special areas is given in Table 8.2-3.

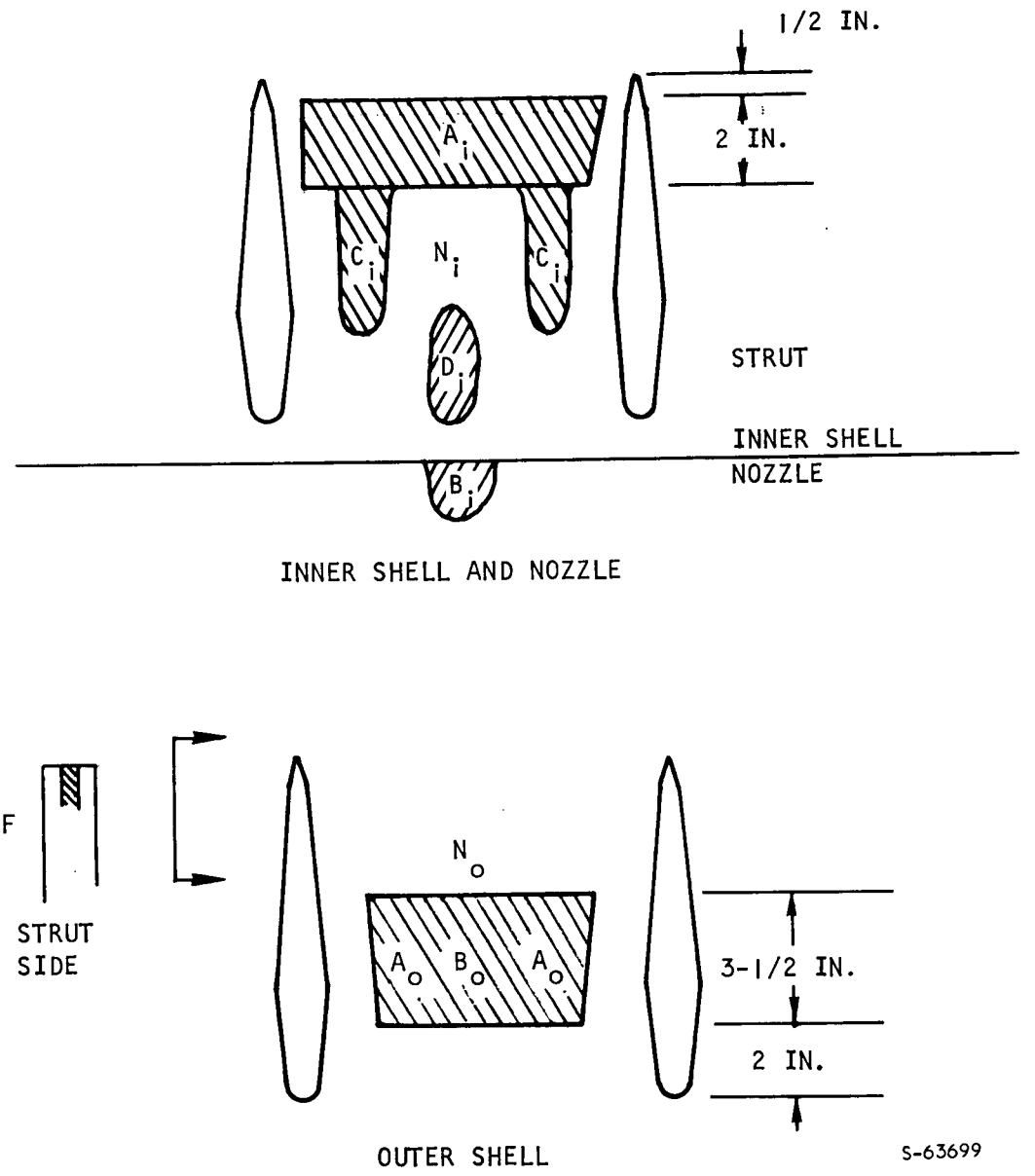

Figure 8.2-5. Some Discolored Areas As Observed After Run 36, Test 42

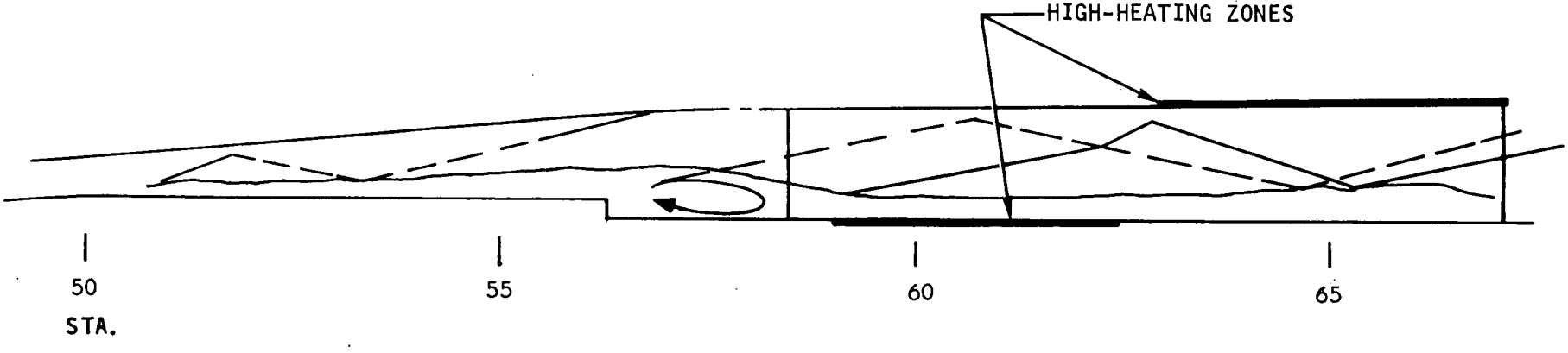

Figure 8.2-6. Estimated Flow Fields Produced by the Aft-Facing Step, Test 41, Run 20

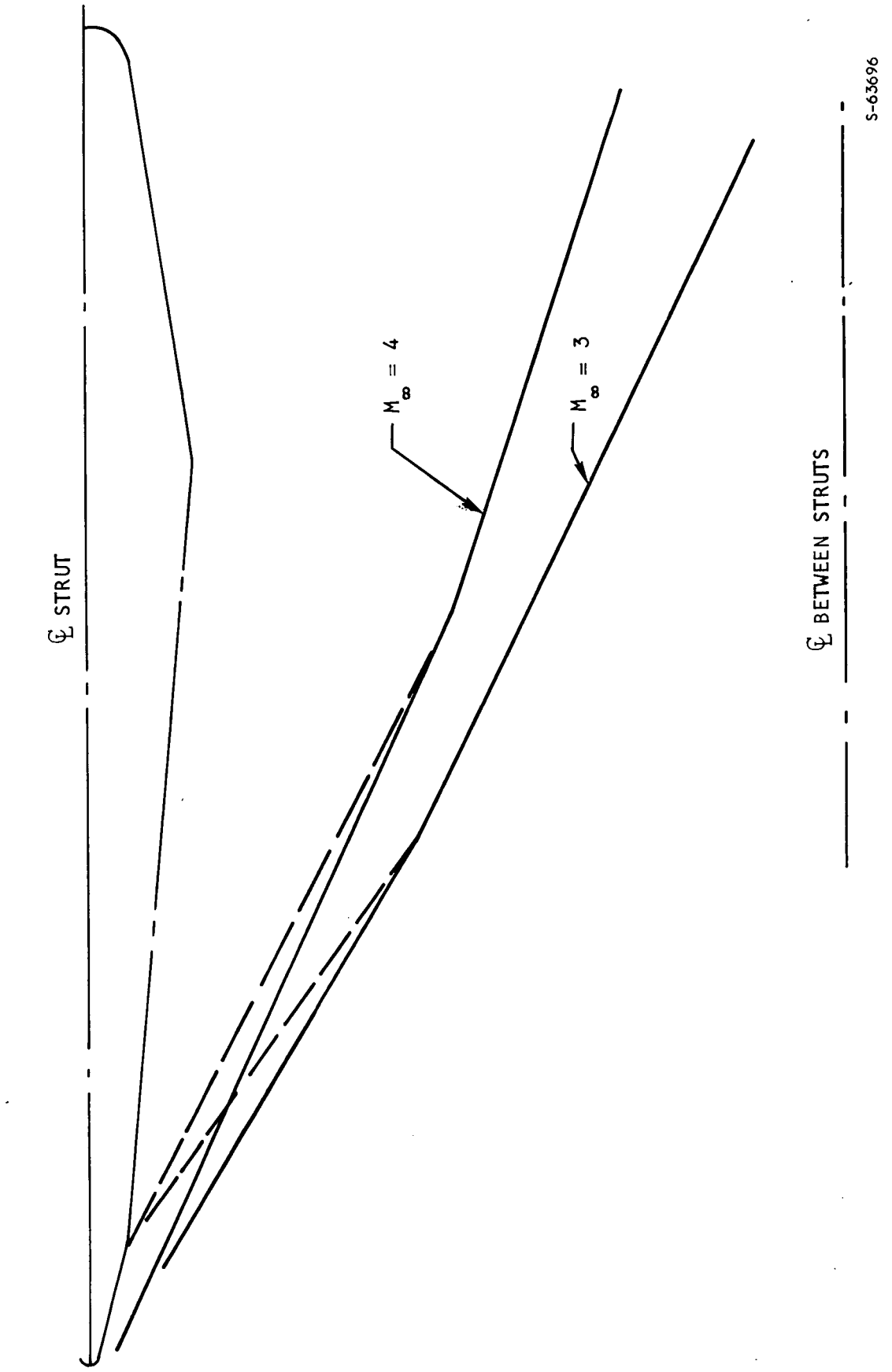

Figure 8.2-7. Flow Field Produced by the Strut

TABLE 8.2-3

ESTIMATED INCREASED HEATING DUE TO SHOCK IMPINGEMENT

Locations	Mach No. Upstream of Shock	Mach No. Downstream of Shock	Overall Pressure Rise Across Shocks	Type of Flow	Heat Transfer Coefficient Increase
Spike, X = 40	4.78	3.85	2.9	No separation	1.7
Inner shell area, A_i, in Figure 8.2-5	4.5	4.1	1.6	Base flow	2-times the value upstream of the spike step
Nozzle area, B_i, in Figure 8.2-5	4.5	-	5.0	Shock impingement	3.0-times the value at N_i, Figure 8.2-5
Outer shell area, A_o, in Figure 8.2-5	4.8	-	4.0	Shock impingement	2.5-times the value at N_o, in Figure 8.2-5
Outer shell area, B_o, in Figure 8.2-5	4.8	3.8	3.0	No separation	1.8
Strut side area, in Figure 8.2-5	4	-	-	3-dim. shock	1.5-times the two-dimensional wedge value

8.2.2 Hydrogen Cooling

For the test runs performed to date, the indicated hydrogen heat load percentages among the five SAM flow routes do not agree with the design point predicted values at 3300 psia, 3600°R tunnel total conditions. The following tabulation shows the indicated hydrogen heat loads and percentages for Test 41, Run 20 (1540 psia, 2700°R) just prior to spike extension after 45 seconds of run time.

	Spike	Leading Edge	Inner Body	Trailing Edge	Struts	Total
H_2 heat load, Btu/sec	403	430	24	44	10	911
Percent of H_2 Heat Load	44.2	47.2	2.6	4.9	1.1	100
Predicted percent at design point	30.8	38.0	11.0	15.4	4.8	100

The heat load percentages on the aft routes (inner body, trailing, edge, and strut sides) are much lower than the design point percentages. There are two reasons for these lower indicated aft-route heat loads. First, the captured hot gas mass flow is less than predicted. The spike retraction for Test 41, Run 20, and therefore, the capture flow ratio is less than that at the design point prediction for shock-on-lip. Shock-on-lip operation requires a spike retraction of approximately 3.9 in. at Run 20 tunnel conditions, versus 2.9 in. Also, Schlieren photographs of the spike bow shock wave in the vicinity of the cowl leading edge indicate that the capture mass flow is less than predicted at 2.86 in. spike retraction. It is estimated that the net reduction in heat load to the aft routes due to lower capture flow is about 20 to 30 percent.

Secondly, the transient heat absorption of the aft routes is producing the most significant reduction in indicated heat load as measured by the hydrogen flow heatup. This can be exemplified by the following calculations. For Test 41, Run 20, the area-averaged structural and hot-wall temperature of the inner body after 45 sec of run time is estimated at 900°R. From the estimated inner body mass of 40 lb, the average heat rate required to raise the inner body temperatures from 500° to 900°R is

$$Q = MCp \frac{\Delta T}{\Delta \theta} = 40 \text{ lb} \times 0.10 \frac{\text{Btu}}{\text{lbm}^{\circ}\text{R}} \times \frac{(900 - 500)\ ^{\circ}\text{R}}{45 \text{ sec}}$$

$$= 35.5 \text{ Btu/sec}$$

This heat rate was estimated with an average temperature rise of 9°R/sec. Inspection of a few inner body structural temperature histories indicate temperature rise rates of 20°F/sec or higher over short durations. Thus, for short durations the heat absorption is likely higher than 35.5 Btu/sec. After 45 sec, inner body structural temperatures were still increasing at a rate of 5° to 10°R/sec. An aerodynamic heating analysis of the inner body for Test 41,

Run 20, based on measured tunnel conditions and static hot gas pressures, indicates a steady-state heat load of 55 Btu/sec. With an average inner body heat absorption rate of 35 Btu/sec, the expected hydrogen heatup should be 20 Btu/sec. From the computed data listings for Test 41, Run 20, the inner body hydrogen heat load is approximately 15 to 20 Btu/sec for the last 20 sec of the 45-sec run time, confirming that the inner body hydrogen heat load is about one-third of the hot gas heat load. During the transient heat-up period, the hydrogen is locally absorbing almost all of the hot gas heat load (less the heat absorption of the 0.015-in.-thick hot wall) but is transferring two-thirds or more of this heat load to the 0.060-in.-thick structural wall and other structure before leaving the flow route.

The inner body flow rate for the above example (Test 41, Run 20) was approximately steady at 0.014 lb/sec. Most of the thermal-cycling test runs have been performed with inner body flow rates reduced to 0.0020 lb/sec or less. With these reduced flows, the disparity between the hot-gas heat load and the hydrogen heat load is greatly increased. The reduced flow rate in the hydrogen heat load equation ($WC_p\Delta T$) is not offset by an increased hydrogen ΔT. The hydrogen ΔT is not substantially increased because the hydrogen heat transfer coefficient is lower.

The hydrogen heat loads on the spike and leading edge flow routes reached steady state for almost all thermal performance test runs. Typically, the hydrogen outlet temperatures for these routes steadied out after 20 to 30 sec into the run. There is good agreement between spike hydrogen heat load and the aerodynamic heat load as calculated from tunnel conditions and measured static pressures. For Test 41, Run 17 (1290 psia, 2700°R), the spike steady-state hydrogen heat load was 360 Btu/sec. The calculated aerodynamic heat load was 414 Btu/sec, or 15 percent higher than measured. Alternate selection of the laminar-turbulent boundary layer transition point and/or using a slightly reduced captured mass flow, as discussed above, could bring the measured and calculated heat loads in to closer agreement.

8.2.3 Metal Temperatures

8.2.3.1 Steady-State Temperatures

Hot wall thermocouple inserts are located at 13 locations on the SAM. These inserts extend through the plate-fin hydrogen passages. They do not record true hot-wall temperature adjacent to the hot gas since the thermocouple junction is still 0.015 to 0.020-in. beneath the surface. Adjacent to these inserts are thermocouples attached to the 0.060-in.-thick or 0.015-in.-thick (nozzle and leading edge outer surface) cold structural wall. These thermocouple pairs have been calibrated analytically so that with a pair of recorded temperatures and the hydrogen flow rate in the plate-fin passage, a hot-wall temperature adjacent to the hot gas and in the vicinity of the insert can be calculated. The calibration, which is applicable for steady-state only, was obtained by thermally modeling the insert and plate-fin passage into a nodal network. Insert junction-to-cold wall temperature difference was calculated on a thermal analyzer computer program for several input hot gas heat fluxes, coolant passage flow rates, and coolant temperatures. Results of the parametric

study were correlated and stored in tabular form in the computer program used to reduce the test data.

Figure 8.2-8 presents the calculated hot-wall temperature at Station 50.40 (reference coordinates) on the outer body for Test 41, Run 17 (1290 psia, 2700°R). Included are the measured insert and cold wall temperatures (T67 and T68) at this location on which the calculation was based. It is noted that the calculated hot-wall temperature adjacent to the hot gas is lower than the insert temperature, T67, even though the insert junction is 0.015 to 0.020 in. beneath the surface. This results from a larger hot-wall-to-structure thermal conductance through the fins than through the insert. The calculated hot-wall temperature is 1370° versus 1430°R for the insert thermocouple reading.

A byproduct of the hot-wall calculation procedure is the hot-gas heat flux which is also indicated in Figure 8.2-8. The average heat flux between 54 and 80 sec is 27 Btu/sec ft^2. A calculation of the aerodynamic heat flux at this outer body location was made using measured tunnel conditions and wall static pressures. Using fully turbulent duct flow relations and the adiabatic wall reference temperature method (discussed in Section 8.2.1), the resulting heat flux is 28 Btu/sec ft^2.

8.2.3.2 Transient Temperatures

Starting with Test 41, Run 26 (2200 psia, 3100°R), metal discoloration caused by metal temperatures of 1000°F or higher was observed on the nozzle at the nozzle/inner shell interface, the outer shell between the struts, and on the first wedge of the struts near the strut leading edge. A detailed description of these locations is discussed in paragraph 8.1.2. A discussion of the aerodynamic phenomena causing the local high heating is presented in paragraph 8.2.1. Transient heat transfer analyses were performed at these locations to verify these observations with predicted temperatures based on test measurements. Results are discussed below.

An analytical heat transfer model of a plate and fin structure and the derivation of the transient hot-wall response for a step-change in hot gas heating and ramp-change in hydrogen coolant temperature is presented in the Appendix. The predicted hot-wall temperature history for the nozzle discolored region (Test 41, Runs 26 and 28) is presented in Figure 8.2-9. Operating conditions for Runs 26 and 28 are similar, except the spike retraction time was 9 sec for Run 26 and 30 sec for Run 28. The hot gas heat transfer coefficient on the nozzle in the absence of local high heating was estimated at 0.013 Btu/sec ft^2-°R. A factor of three was applied to this coefficient to account for the local heating (i.e., 0.040 Btu/sec ft^2-°R). The hydrogen heat transfer coefficient, 0.078 Btu/sec ft^2-°R, was based on a near constant inner body flow rate of 0.0045 lb/sec. The nozzle outlet hydrogen temperature, T54, was assumed to be equal to the local hydrogen temperature history at the discolored region and was approximated by a constant slope of 10°R/sec. The predicted nozzle hot wall temperature for Run 26 is 1540°R (1080°F) and 1685°F

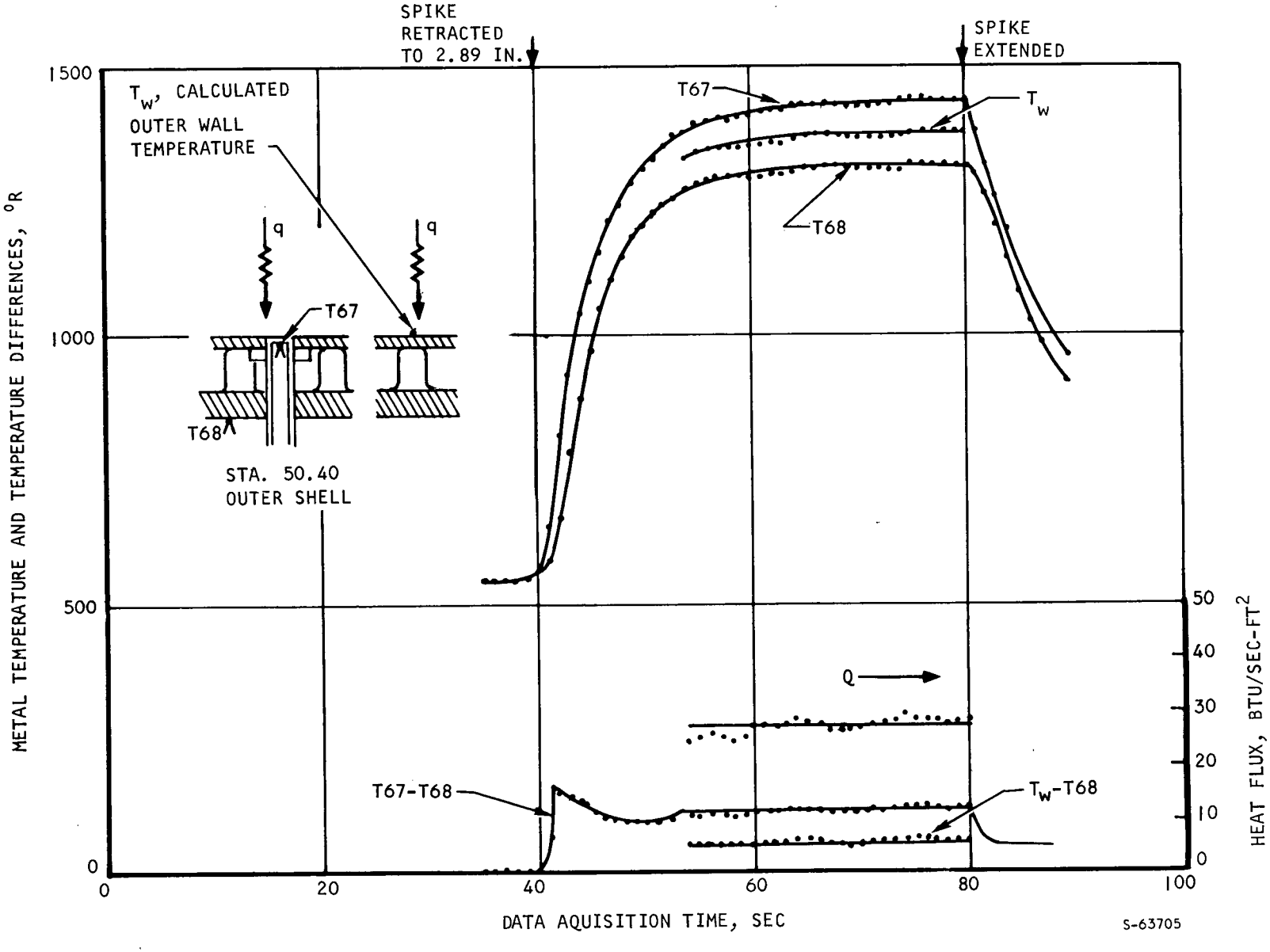

Figure 8.2-8. Corrected Hot Wall Temperate Calculation, Outer Shell, Test 41, Run 17 (1290 psia, 2700°R)

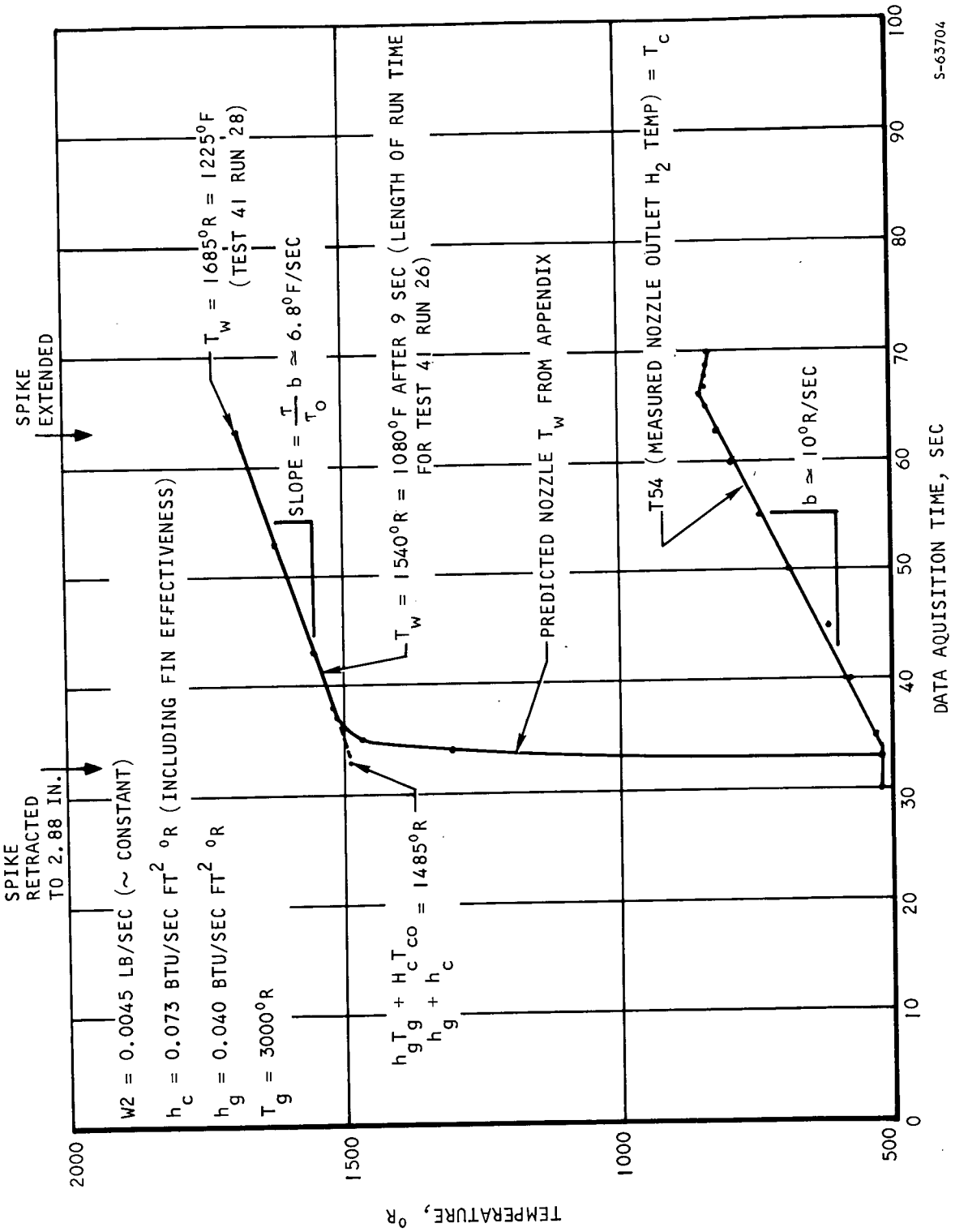

Figure 8.2-9. Nozzle Hot Wall Temperature Response, Test 41, Runs 26 and 28 (2200 psia, 3000°R)

(1225°F) for Run 28. Both of these temperatures will produce metal discoloration as discussed in paragraph 8.1.2.

A similar calculation was performed on the outer shell discolored location between the struts. Results for Test 41, Run 26, are presented in Figure 8.2-10. The predicted wall temperature reached 1510°R (1050°F) after 9 seconds. For Run 28, the predicted hot-wall temperature was estimated at 1800°R (1340°F). Included for comparison in Figure 8.2-10 is T92, the hot-wall insert temperature at approximately the same axial location (62.30 reference coordinates) on the outer shell as the predicted hot-wall temperature but not in the local high-heating region.

The strut-sides hot-wall temperature along the first wedge was estimated at 1500°R (1040°F) for Test 41, Run 28. Though this predicted temperature is sufficient to cause some discoloration, it is not at all unexpected since the predicted temperature at the 3300 psia, 3600°R tunnel conditions is 1900°R (1440°F) in Reference (8-2).

Metal discoloration at these three locations was also observed after thermal cycling test runs (1380 psia, 2700°R) with hydrogen injection. Though the total pressure is less than during Test 41, Run 26 (2200 psia), wall hot-gas static pressures on the aft routes were indicating approximately 60 percent higher than comparable runs without injection. This suggests that combustion is occurring. The extent of the combustion has not been investigated nor its impact on heating determined in terms of total-temperature changes. Considering the increase in static pressure only, however, results in increased heating on the aft routes sufficient to explain the discoloration in the areas in which it was observed.

8.3 STRUCTURAL PERFORMANCE

8.3.1 Pressure Loading

The engine shell structures and the manifold ring structures were designed to withstand aerodynamic loading due to axisymmetric and asymmetric engine unstarts at 1800 psf dynamic pressure and M_∞ = 8.0 operating conditions. The aerodynamic loading in the SAM tunnel tests was estimated to be 25 to 30 percent of the engine design load at 3300 psia total pressure. Potential load intensities for the tests conducted to date are less than this.

The strain gage data from the SAM tests was reviewed for several of the runs, and total loads appeared to be quite small based upon the low stresses that were measured. This has provided verification that the engine has not been exposed to structural damage in the load-carrying structure. The future data reduction effort in this area will be directed toward a thorough evaluation of several of the higher total-tunnel pressure runs. Although the various strain gage bridge networks on the spike and the actuator structures were calibrated strictly for lateral loading and applied bending moments, it should be possible to make some estimates of total axial loadings developed on the spike and actuator during the test sequence from these bridge readings.

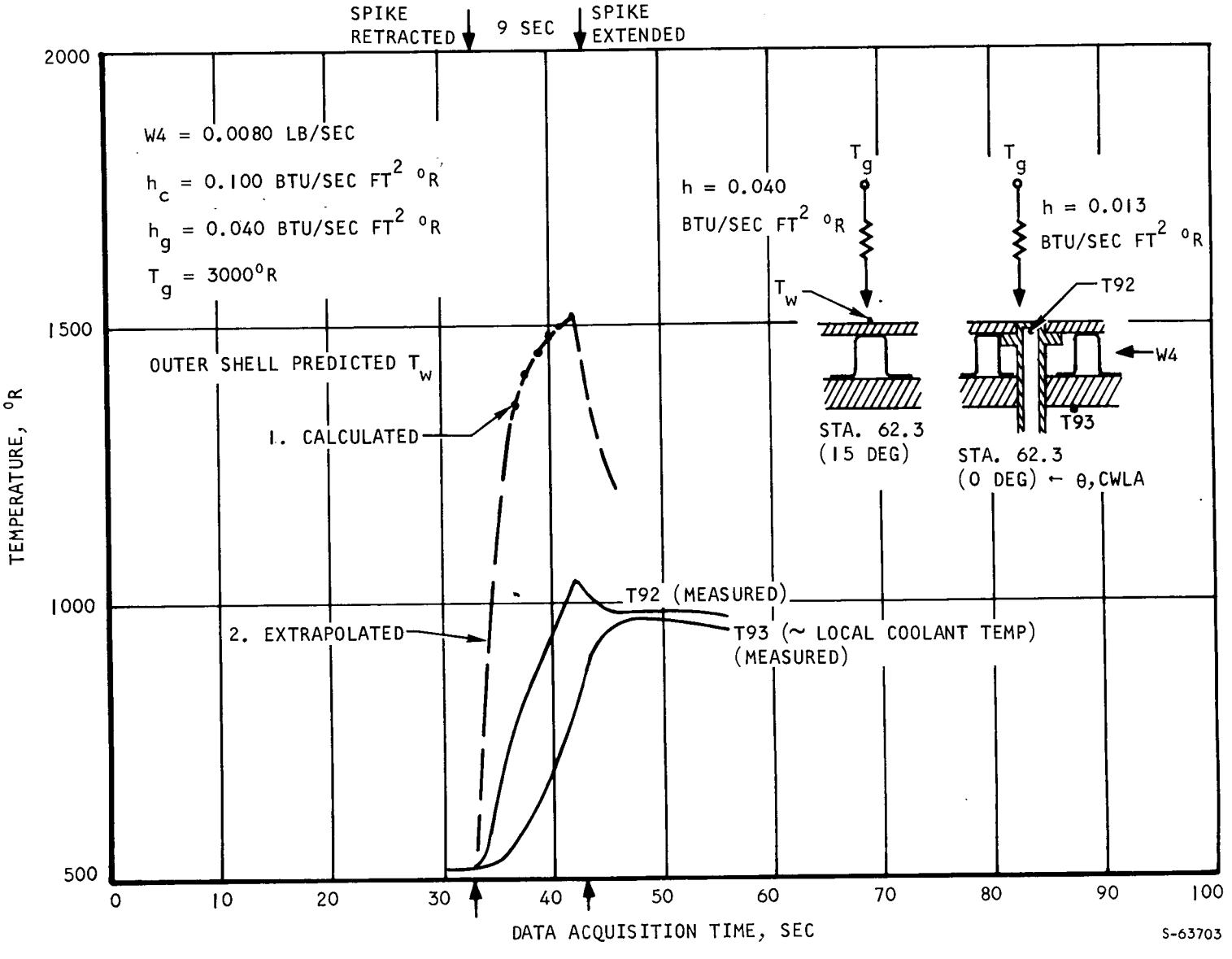

Figure 8.2-10. Outer Shell Hot Wall Temperature Response, Test 41, Run 26 (2200 psia, 3000°R)

8.3.2 Dynamic Loading

Thirteen directional accelerometers were installed in the engine to monitor accelerometer response magnitudes during tunnel testing. The accelerometer data for the various test runs have been subjected to power spectral density (PSD) analysis in order to assess engine resonant frequencies and major forcing frequencies applied to the engine.

The engine was designed to the work statement requirement calling for a 3-g input loading at the engine mount points in each of three perpendicular axes. In addition, the engine was also originally designed to withstand maneuver loads, aerodynamic loads and simultaneous vibrational loads as specified in the statement of work. The vibratory and maneuver loads would have been imposed at the engine attachment points by the intended flight test airplane, the X-15-2A. As a consequence of the various load conditions and combinations, the engine was essentially designed to withstand a 20-g axial load factor applied to the entire engine. For lateral or vertical loads, the engine was designed to meet a 20-g load factor applied to the spike and its supported contents and a 7.5-g load factor applied to the inner body and outer body of the full flight engine. Since the SAM does not contain all of the equipment that would have been installed in the flight engine, the SAM is somewhat lighter than the latter.

Some accelerometer data has been processed and this data shows the maximum acceleration responses during the tunnel runs to be well below 7.5 g except for some local and short-duration impulsive loads. The PSD data reduction has indicated a distinct driving frequency at 27 cps during the tunnel runs. In general, the magnitudes of the acceleration loads appear to be well within the structural capability of the engine. A more detailed evaluation remains to be performed in order to determine mode shapes and principal resonant loadings on the various portions of the supporting structure. In the remaining data evaluation effort, attention will be directed toward the determination of mechanical loadings due to dynamic effects.

8.3.3 Low-Cycle Fatigue

One of the major areas of interest has been the evaluation of thermal fatigue damage accumulated to date. Based upon prior mechanical bending fatigue tests and thermal fatigue cycling tests on plate-fin specimens, as well as the application of the techniques of low-cycle fatigue analysis, the SAM engine was designed to a specific target objective. The hot skin has a design life goal of 100 cycles for steady-state operating differential temperatures of 800^{0}F with a hot skin temperature of 1600^{0}F and a structural wall temperature of 800^{0}F. The actual calculated life of the engine at these conditions was 136 cycles.

In the SAM test procedures, the engine is rapidly injected into the tunnel gas stream after tunnel startup to begin a test cycle, and it is rapidly retracted prior to tunnel shutdown. The rate of change of heating loads is much greater than the thermal response rate of the structural elements of the engine. The heated outer skins respond almost instantly to the heating. It is because of this response characteristic that it is possible to produce large differential

temperatures on the engine heated surfaces during the tunnel tests, even though steady-state temperature differentials would be much less than the original design conditions. A second favorable factor was the rapid cooldown of the outer skins after engine retraction. The surface metal temperature has achieved negative differentials relative to the structural metal of up to 400°F during several of the test runs. Since the total thermal fatigue effect is due to the summation of the positive and negative temperatue differentials during each full thermal duty cycle, this factor has greatly facilitated the achievement of measurable and substantial cumulative thermal fatigue damage during the test sequence to date.

A specific series of tests has been carried out during the test program to date for the main purpose of thermal fatigue damage accumulation; i.e., Test 42, Runs 19 through 33. However, some thermal fatigue damage is accrued during each engine injection/retraction cycle. The total test program may be realistically viewed as a continuous series of events with respect to the accumulation of thermal fatigue. The time intervals between tests and the specific functional test objectives of each different run are not factors in the determination of fatigue damage at the locally heated areas of consequence. The only data of significance is the time/temperature history at the most heavily loaded engine locations from the first test to the last test performed to this date.

Before the start of testing, calculations were performed to assess temperature differential time history at several critical areas in the engine. This analysis revealed that the two most critical areas in the engine would be the hot skin, directly adjacent to the outer body outlet manifold, and the hot skin on the strut side walls. A number of thermocouples had been installed to measure outer body outlet manifold temperature and hot skin temperature next to the manifold. Although several thermocouples had been installed within the strut bodies, there were no hot skin thermocouples on the struts. It was decided to somewhat depress the temperature differentials in the struts by means of a modest amount of overcooling. In this way the most critical area of the engine would be that portion with the most complete instrumentation. This approach does not guarantee that the outer body outlet manifold region has been the most severely thermally loaded part of the entire engine. It does enhance the data evaluation at this location as being a valid indicator of fatigue damage during the test program. The calculated fatigue damage fraction at this location is therefore believed to be a true measure of thermal fatigue, although other areas in the engine may have been exposed to somewhat greater damage.

One objective of the test program was to conduct a substantive evaluation of engine fatigue performance. However, another basic ground rule that was imposed was to avoid undue risk in damaging the engine. The thermal test sequence was then devised to produce a calculated damage fraction of 0.40 to 0.60. Note that a damage fraction of 0.50 would require 68 duty cycles at the original design conditions, which would in turn be 68 percent of the intended design life of 100 operating cycles.

The test summary, Table 8.1-1, shows the pertinent test conditions. Also shown on this table were the arithmetic summations of the positive and negative

temperature differences during each duty cycle, the total thermal expansion differential during each cycle, and the damage fractions associated with each thermal cycle. The damage fractions shown, are (1) the inverse of the number of cycles to fail at each condition, and (2) the accumulated damage to each run.

The approach taken to calculate thermal fatigue damage has been based upon the previous work to date. Low-cycle fatigue damage follows a power function law that can be related to plastic strain and material ductility properties as follows:

$$N = \left(\frac{C}{\Delta\epsilon_p}\right)^k$$

Where

N = cycles to fail

C = ductility constant

$\Delta\epsilon_p$ = plastic strain amplitude

k = exponent

Extensive investigations have been conducted in recent years, and total agreement among the various investigators has not as yet been achieved. Following the lead of several of the principal contributors to the subject, the previous test data reduction was directed toward assessing reasonable values for C and k to use in the present analysis. Excellent results were obtained that produced substantial agreement between the mechanical and the thermal specimen tests by using $k = 2.0$. The value for C is a function of temperature. Tests had been carried out at room temperature, at 1340°F, and at 1540°F. No discernible difference was noted between the test results at 1340° and 1540°F, but substantially greater life was obtained at room temperature. The lower fatigue life at elevated temperature must be ascribed primarily to the effects of creep, since ductility data on parent metal specimens were not notably different at the three temperatures. Actually, a slight increase in ductility occurs with Hastelloy X at 1540°F, as compared to 1340°F, and this increased ductility appears to offset the higher creep damage at 1540°F. For the purposes of analysis, a method was required to account for the decreased fatigue performance between room temperature and 1340°F. Since the true relationship is not known, it was decided to employ a linear variation in ductility constant between these temperature extremes which actually represents a second order or parabolic relationship in terms of cycles-to-fail. The formulas also automatically account for localized strain concentrations due to the plate fin configuration as well as ductility reductions due to the influence of braze alloying, and braze processing on the structure. This is true because the constants were evaluated from the thermal and mechanical test data on plate-fin specimens that simulated the design and processing of the cooled engine structures.

The fatigue life formulations are:

$$N = \left[\frac{0.150 - 0.050\,\frac{(T_{max} - 530)}{(1270)}}{\Delta\epsilon_p}\right]^2 , \quad 76^0F < T_{max} < 1340^0F$$

$$N = \left[\frac{0.100}{\Delta\epsilon_p}\right]^2 , \quad T_{max} \geq 1340^0F$$

The effect of maximum test temperature on the ductility constant is shown in Figure 8.3-1 while the effect on cycles-to-fail with a nominal plastic strain amplitude of 0.010 (one percent) is shown in Figure 8.3-2.

It was finally necessary to obtain a relationship between thermal differential expansion and plastic strain amplitude. Since the hot surface is constrained from growth, both axially and circumferentially, curves were developed representing the total equivalent plastic strain from the Hencky-Mises relationship as a function of bi-axially applied strain deformations. The formulations utilized the actual stress-strain properties of the material, thereby accounting for strain hardening. Allowance was also made for the elastic deformations of the structural material to which the hot surface is bonded. Although this contribution was small, it was not entirely negligible. The calculation was performed for several temperatures. It was found that within the temperature range of interest, the elastic modules decreased at almost the same rate as the elastic strength properties, and that the elastic strain component of the heated surface was virtually independent of temperature. An excellent fit within the range of interest applicable to temperature differentials ranging from 300^0 to 1200^0F was produced by the following formula:

$$\Delta\epsilon_p = 1.75 \sum(\alpha\Delta T) - 0.0050$$

where

$\Delta\epsilon_p$ = equivalent plastic strain

$\sum(\alpha\Delta T)$ = total differential expansion due to positive and negative effects.

These formulas were applied to each test cycle to obtain the calculated results shown in Table 8.1-1.

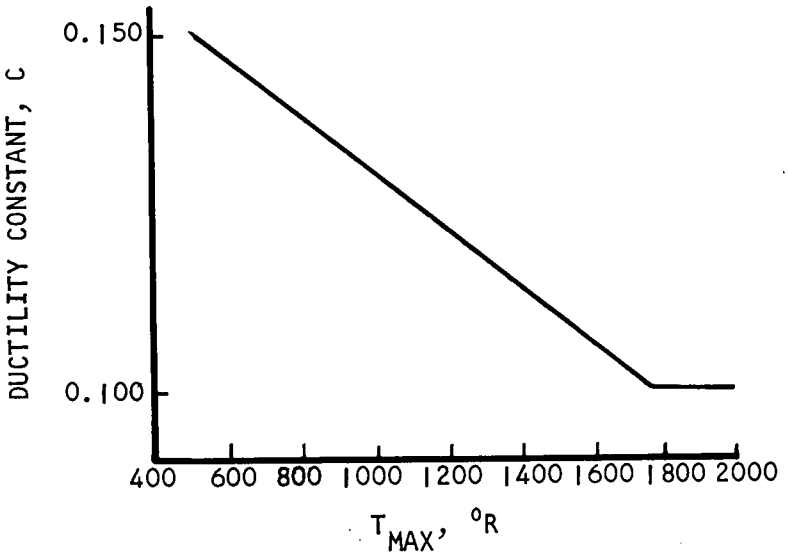

Figure 8.3-1. Ductility Constant vs Temperature

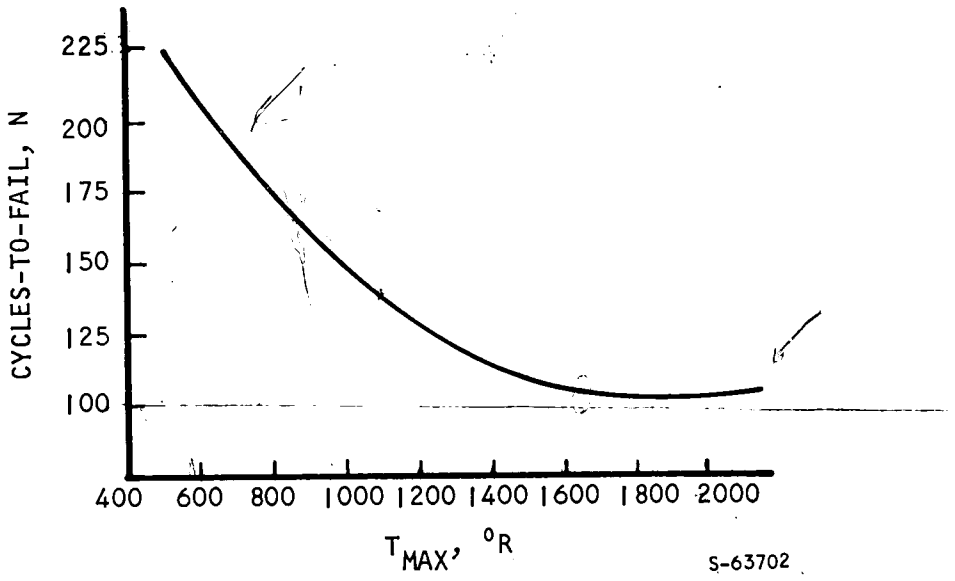

Figure 8.3-2. Cycles-to-Fail vs Maximum Hot-Wall Temperature With Assumed One-Percent Plastic Strain

8.4 SUMMARY

8.4.1 Heat Transfer

Preliminary aerodynamic heating and hydrogen cooling data reduction and analyses have been performed for SAM tests. Aerodynamic heating correlations on the spike, cowl leading edge, and inner shell are in fair agreement with the experimentally determined hydrogen heat loads. The adiabatic wall reference-enthalpy method for evaluating boundary layer transport properties gives better agreement that Eckert's reference-enthalpy method. Correlation of aerodynamic heating and hydrogen cooling on the nozzle, aft outer shell, and strut sides is unsatisfactory for the test data to date. Non-attainment of thermal steady-state, hot gas shock interference patterns, and hydrogen flow rate uncertainties in these routes have contributed to the complexity of a comparison.

The propogation of shock interference patterns in the vicinity of the struts are of larger intensities than predicted. These shock patterns produced local high-heating zones on the strut sides, aft outer shell between the struts, and on the nozzle at the inner shell joint, halfway between struts. Local heating levels were from 1.5-(strut sides) to 3-(nozzle) times the average predicted levels for these areas.

Non-attainment of thermal steady state on the inner body, aft outer shell, and strut sides, has disguised the hot gas heat loads as measured by hydrogen heatup. For most tests to date, the hydrogen heat load was, at most, indicating only one-third of the inner body hot gas heat load. At higher tunnel total pressures (2700 psia and higher) and the associated higher hydrogen flow rates, transient time responses of the aft routes are expected to be less than 30 sec and permit better estimates of heat load.

When the local heating effects due to shock interference patterns are considered, metal temperature predictions of 1050°F on the strut sides (on the first wedge directly behind the leading edge), 1225°F on the nozzle, and 1400°F on the outer shell are in reasonable agreement with the observed metal discolorations.

8.4.2 Structural

Structural loads due to pressure and vibrational effects have been well within the structural capability of the engine. Further detailed data reduction is required to assess load magnitudes and distribution.

The evaluation of thermal fatigue has been completed through Test 42, Run 36. The accumulated damage fraction is 0.278. The balance of the tests include several at heating conditions that will be more intensive than any of the runs to date. The cooling rates will be increased to accommodate these higher heat loads. The maximum thermal differentials will still be a function of coolant flow rates and time exposure in the tunnel. It now appears that the initial test objective of a computed total-fatigue damage fraction of 0.40 to 0.60 can be accomplished. Each run will be analyzed upon completion to ascertain that excessive damage is not produced in any single run.

An area that remains open to further attention is investigation of thermal fatigue in parts of the engine that have not been fully instrumented but are known to have been exposed to severe heat loading. One such typical example is the nozzle region that has been heated to fluxes well above the nominal heat load due to shock interactions.

8.4.3 SAM Condition

The condition of the cooled structure was satisfactory following the tests to date. Leakage encountered has not affected operation or resulted in local overheating. Moreover, leakage and denting of the leading edge due to foreign object impingement indicates considerable tolerance to such damage.

No leaks have been observed in the hot skins as a result of thermal cycling; i.e., fatigue cracking. Leakage around the struts and at the aft end of the inner shell may be associated with cycling of the joints in these areas. As noted above, relative heating rates (local heat flux to average heat flux) are quite high in these areas and may be in excess of the design ratios during the fuel injection runs. During these runs, there was some combustion of the injected hydrogen.

The test systems associated with the SAM have functioned satisfactorily. The water systems show good cycling performance and no indication of damage. The temperature and pressure control systems have performed well in terms of both the control and failsafe functions. The inlet spike actuation control system has functioned well and shown good repeatibility, as determined in periodic calibrations against spike position. Pneumatic valves have required expected adjustments of venting to compensate for low tunnel statics, but have shown adequate response. The five turbine flowmeters in the hydrogen system show excellent agreement of calibrations before the test and following Test 42, Run 36. At this time, the inner body and aft outer shell flowmeters were removed and calibrated against standard nozzles. The main, leading edge, and spike flowmeters were calibrated in place, using a calibrated venturi as reference.

9. FUTURE ACTION

Testing of the SAM will continue in the NASA Langley 8-Foot High Temperature Structures Tunnel. A series of eleven more runs is planned. Tunnel total conditions will be increased to a maximum of 3300 psia and 3600^{0}R. For the high pressure and temperature runs, cryogenic hydrogen will be used as the coolant. In addition to the general increase in severity of the runs, specific tests with spike shock on the cowl lip are planned as part of the remaining program.

Following completion of the tests, data analysis will continue and preparation of the test report will be started.

REFERENCES

8-1 Hypersonic Research Engine Project - Phase II, Structures Assembly Model Test Plan , Data Item No. 64.01, AiResearch Report AP-70-6120, 11 March 1970

8-2 Hypersonic Research Engine Project - Phase IIA, Structures and Cooling Development Ninth Interim Technical Data Report, Data Item No. 55-7.09, AiResearch Report AP-69-5075, 3 June 1969

APPENDIX

PLATE-FIN HOT WALL TEMPERATURE RESPONSE

Form 2427

AIRESEARCH MFG. CO.

DATE_____ CALC. NO._____

PREPARED BY_____ MODEL _____

CHECKED BY_____ PART NO._____

APPENDIX

PLATE-FIN HOT WALL TEMPERATURE RESPONSE

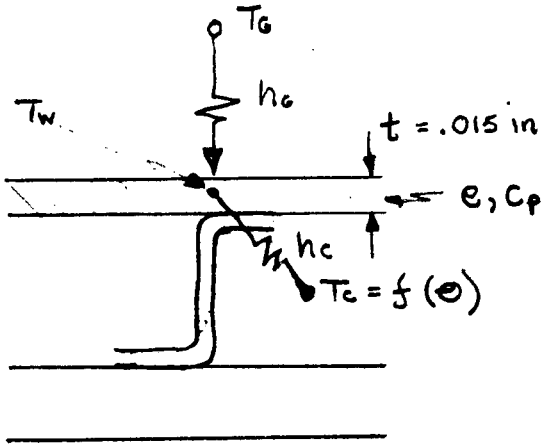

Conditions:

1. Step change in hot gas heating at $\theta = 0$
2. Constant coolant flow rate
3. Ramp change in coolant temp.

θ = time, sec

$e = 0.30$ lbs/in^3

$C_p = 0.10$ Btu/lbm°R

h_G = hot gas heat transfer coefficient

h_c = coolant heat transfer coefficient (includes fin effectiveness)

T_G, T_w, T_c = hot gas, hot wall, and coolant temp.

A heat balance on a unit area of surface is

$$h_G (T_G - T_w) - h_c (T_w - T_c) = e C_p t \frac{d T_w}{d\theta} \qquad (1)$$

Introducing $T_c = T_{co} + b\theta$ (b = constant coolant temp slope and rearranging gives,

AiRESEARCH MFG. CO.

DATE_____ CALC. NO._____
PREPARED BY_____ MODEL _____
CHECKED BY_____ PART NO._____

$$\frac{d T_w}{d\theta} + \left(\frac{h_g + h_c}{e c_{pt}}\right)\left[T_w - \frac{h_g T_g + h_c T_{co}}{h_g + h_c} \right] = \frac{h_g b}{e c_{pt}} \theta \qquad (2)$$

Let $$T_w^* = T_w - \frac{h_g T_g + h_c T_{co}}{h_g + h_c}$$

$$\tau_c = \frac{e c_{pt}}{h_c} \quad , \quad \tau_g = \frac{e c_{pt}}{h_g}$$

and $$\frac{1}{\tau} = \frac{1}{\tau_c} + \frac{1}{\tau_g}$$

Then Equation (2) becomes

$$\frac{d T_w^*}{d\theta} + \frac{T_w^*}{\tau} = \frac{b}{\tau_c} \theta \qquad (3)$$

Two items are noticed at this point:

1. The quantity $(h_g T_g + h_c T_{co}) / (h_g + h_c)$ is the steady state wall temperature (T_{co} is the coolant temperature) was maintained constant at T_{co}.
2. τ_c and τ_g can be considered as the wall time constants when the wall is exposed to the coolant and hot gas, separately. When exposed to both heating and cooling, the reciprocal of the time constants are additive, i.e. $\frac{1}{\tau_c} + \frac{1}{\tau_g} = \frac{1}{\tau}$. The net result is a time constant less than the individual time constants.

AiRESEARCH MFG. CO.

DATE_____ CALC. NO._____
PREPARED BY_____ MODEL _____
CHECKED BY_____ PART NO._____

The solution of Eq. (3) is

$$T_w^* = e^{-\theta/\tau}\left\{\frac{b}{\tau_c}\int \theta e^{\theta/\tau}\, d\theta + C\right\}$$

or

$$T_w^* = e^{-\theta/\tau}\left\{\frac{b}{\tau} e^{\theta/\tau}\left[\tau\theta - \tau^2\right] + C\right\} \qquad (4)$$

where C is an integration constant. With boundary conditions that

at $\theta = 0$, $T_w = T_{wo}$

or $T_{wo}^* = T_{wo} - \dfrac{h_G T_G + h_c T_{co}}{h_G + h_c}$

then

$$T_w^* = b\left(\frac{\tau}{\tau_c}\right)(\theta - \tau) + \left[T_{wo} + b\left(\frac{\tau}{\tau_c}\right)\tau\right] e^{-\theta/\tau} \qquad (5)$$

For $\theta \gg \tau$ (usually $\theta/\tau > 4$) the exponential term approaches zero so that

$$T_w^* = T_w - \frac{h_G T_G + h_c T_c}{h_G + h_c} \simeq b\left(\frac{\tau}{\tau_c}\right)(\theta - \tau)$$

For the nozzle conditions for Test 41, Run 26 (see Figure 8.2-2)

$h_G = 0.040$ Btu/sec.ft^2°R

$h_c = 0.073$ Btu/sec ft^2°R (WIB = .0045 lbs/sec)

$\rho c_p t = 0.0648$ Btu/ft^2·°R (t = .015 in)

$b = 10$ °R/sec

$T_{co} = 500$ °R, $T_G = 3000$ °R

Then

$\tau_c = 0.886$ sec

$\tau_G = 1.62$ sec

$\tau = 0.60$ sec

$$\frac{h_G T_G + h_c T_{co}}{h_G + h_c} = 1485°R \ (1025°F)$$

For $\Theta > 4\tau = 4 \times 0.60 \simeq 2\frac{1}{2}$ sec

$$T_w = 1485 + 10\left(\frac{0.60}{0.866}\right)(\Theta - .60)$$

$$= 1485 + 6.8(\Theta - 0.60)$$

$$\simeq 1485 + 6.8\Theta \quad , \quad \Theta \gg \tau = 0.60 \text{ sec}$$

This prediction for the locally high heated outer wall of the nozzle is plotted in Figure 8.2. It is noted that after $2\frac{1}{2}$ sec (4τ) the wall temperature is essentially tracking the coolant temperature. The slope of T_w is not equal to the slope of T_c since the heat flux is decreasing with increasing T_w. It can be shown that the T_w and T_c slopes would be equal if the heat was constant rather than constant h_G as used herein.